Quantifying internal friction in unfolded and intrinsically disordered proteins with single-molecule spectroscopy

Andrea Soranno[a,1], Brigitte Buchli[a,1,3], Daniel Nettels[a,1], Ryan R. Cheng[b], Sonja Müller-Späth[a], Shawn H. Pfeil[c,4], Armin Hoffmann[a,5], Everett A. Lipman[c], Dmitrii E. Makarov[b,2], and Benjamin Schuler[a,2]

[a]Biochemisches Institut, Universität Zürich, Winterthurerstrasse 190, 8057 Zürich, Switzerland; [b]Department of Chemistry and Biochemistry and Institute for Computational Engineering and Sciences, University of Texas at Austin, Austin, Texas, 78712; and [c]Department of Physics, University of California, Santa Barbara, California 93106

Edited by Peter G Wolynes, University of California, San Diego, La Jolla, CA, and approved February 7, 2012 (received for review October 28, 2011)

Internal friction, which reflects the "roughness" of the energy landscape, plays an important role for proteins by modulating the dynamics of their folding and other conformational changes. However, the experimental quantification of internal friction and its contribution to folding dynamics has remained challenging. Here we use the combination of single-molecule Förster resonance energy transfer, nanosecond fluorescence correlation spectroscopy, and microfluidic mixing to determine the reconfiguration times of unfolded proteins and investigate the mechanisms of internal friction contributing to their dynamics. Using concepts from polymer dynamics, we determine internal friction with three complementary, largely independent, and consistent approaches as an additive contribution to the reconfiguration time of the unfolded state. We find that the magnitude of internal friction correlates with the compactness of the unfolded protein: its contribution dominates the reconfiguration time of approximately 100 ns of the compact unfolded state of a small cold shock protein under native conditions, but decreases for more expanded chains, and approaches zero both at high denaturant concentrations and in intrinsically disordered proteins that are expanded due to intramolecular charge repulsion. Our results suggest that internal friction in the unfolded state will be particularly relevant for the kinetics of proteins that fold in the microsecond range or faster. The low internal friction in expanded intrinsically disordered proteins may have implications for the dynamics of their interactions with cellular binding partners.

energetic roughness | Kramers theory | protein folding | Rouse model | single-molecule FRET

Conformational changes in proteins, including those involved in protein folding, are driven by thermal fluctuations. In the dense environment of an aqueous solution, these processes thus typically exhibit diffusive dynamics (1–4). A theoretical framework for describing such diffusive processes in the condensed phase is provided by Kramers-type theories, which have been successful in quantifying key properties of protein folding reactions (5–12). These theories predict the rate of folding to depend exponentially on the height of the folding free energy barrier, with a prefactor representing the "attempt frequency" of crossing the barrier. The latter is related to the inherent timescale at which the protein can diffusively explore its conformational space. As a result, the reaction rate is expected to depend on the friction (13). For simple reactions, only solvent friction may need to be taken into account, but in proteins, where the amino acid residues are only partially exposed to solvent, other dissipative, "internal friction" mechanisms are possible and result in a slowdown of the conformational dynamics. In particular, intrachain collisions, dihedral angle rotation, and other interactions within the polypeptide chain (1, 14, 15) lead to an increased "roughness" of the underlying energy landscape, thereby slowing conformational rearrangements within the molecule (16). Theory (5, 17), simulation (8, 12, 18–20), and recent experimental results (9, 11, 21–23) all indicate that changes in reconfiguration times due to changes in this internal friction can significantly modulate protein folding dynamics. In particular, the diffusive "speed limit" of the folding reaction (24), which is determined by the rate of reconfiguration of unfolded and nonnative conformations, should also be affected by internal friction.

Classic models of polymer dynamics, such as the Rouse and the Zimm models, present an opportunity to conceptualize the role of internal friction in unfolded proteins. These models provide estimates of the reconfiguration timescale of a polymer chain in a random-coil state given the average size of the coil and its translational diffusion coefficient (25). While in their original form they assume chain dynamics to be controlled only by the viscous drag from the solvent, internal friction can also be included. The analysis of experimental data with such models then allows a conceptually coherent quantification of internal friction. As pointed out above, internal friction effects may be due to a variety of mechanisms. Some of them would result in solvent-mediated ("wet") friction, whose magnitude is proportional to the solvent viscosity (16). Others may lead to "dry" (or Cerf) friction, which is independent of the solvent viscosity (26). Differentiating between such mechanisms is essential for our understanding of the dynamics of the unfolded state, their role in folding, and the function of intrinsically disordered proteins (IDPs) (27, 28). Previous experiments have shown that changes in the dimensions of unfolded proteins or peptides (29–31) can be linked to changes in chain dynamics (21, 32, 33), and a role of internal friction at the transition state for folding has been demonstrated for several proteins (9, 15, 23, 34, 35). However, the contribution of internal friction to unfolded state dynamics has eluded experimental quantification (21, 36). Here we use single-molecule fluorescence experiments to quantify internal friction in unfolded proteins and IDPs.

Author contributions: A.S., D.N., A.H., D.E.M., and B.S. designed research; A.S., B.B., D.N., R.R.C., and D.E.M. performed research; A.S., B.B., D.N., R.R.C., S.M.-S., S.H.P., A.H., E.A.L., and D.E.M. contributed new reagents/analytic tools; A.S., B.B., D.N., R.R.C., and D.E.M. analyzed data; and A.S., D.N., D.E.M., and B.S. wrote the paper.

The authors declare no conflict of interest.

This article is a PNAS Direct Submission.

[1]These authors contributed equally to this work.

[2]To whom correspondence may be addressed. E-mail: schuler@bioc.uzh.ch or makarov@mail.utexas.edu.

[3]Current address: Physikalisch-Chemisches Institut, Universität Zürich, 8057 Zürich, Switzerland

[4]Current address: Pennsylvania Muscle Institute, Perlman School of Medicine at the University of Pennsylvania, Pennsylvania 19104, USA

[5]Current address: Department of Physics, University of Alberta, Edmonton AB T6G 2M9, Canada

This article contains supporting information online at www.pnas.org/lookup/suppl/doi:10.1073/pnas.1117368109/-/DCSupplemental.

Results

Dimensions and Dynamics from Single-Molecule FRET and Nanosecond FCS. Quantifying unfolded state dynamics requires the accurate measurement of both distance distributions and reconfiguration kinetics. Fig. 1 shows a representative set of measurements on the unfolded state of the small cold shock protein from *Thermotoga maritima* (Csp) labeled at positions 2 and 68 with Alexa 488 and Alexa 594 as donor and acceptor, respectively, for Förster resonance energy transfer (FRET). From the FRET efficiency histogram (Fig. 1*A*), the mean transfer efficiency of the unfolded state can be determined and used to calculate the parameters of a suitable distance distribution (37). The good agreement of the observed donor fluorescence lifetimes with the dependence on the mean transfer efficiency *E* expected for a Gaussian or a wormlike chain (Fig. 1*B*, *Supporting Information* and Fig. S1) supports previous measurements that suggest that simple polymer models can provide a reasonable approximation for long-range distance distributions in the unfolded state (29–31, 37–41).

The information on chain dynamics is obtained from nanosecond fluorescence correlation spectroscopy (nsFCS), which allows the fluctuations in distance between donor and acceptor to be monitored (21, 42). The decays of the fluorescence intensity correlation functions (Fig. 1 *C–E*) can be directly related to the reconfiguration time of the polypeptide chain (21, 43, 44), defined as the relaxation time of the distance correlation function (e.g., of the end-to-end distance, if the labels are located at the chain termini).* The resulting end-to-end distance reconfiguration times, τ_r, are in the range of 50 ns to 100 ns. This approach for determining τ_r is the basis for investigating the role of solvent friction and internal friction for chain dynamics.

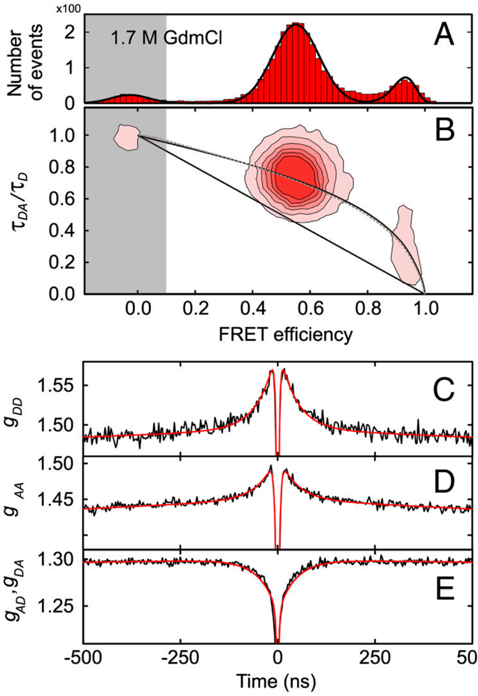

Fig. 1. Unfolded state dimensions and dynamics from single-molecule FRET and nsFCS. (*A*) Example of a FRET efficiency histogram of terminally labeled Csp at 1.7 M GdmCl, with the unfolded subpopulation at $E \approx 0.55$, the folded subpopulation at $E \approx 0.95$, and the donor-only population at $E \approx 0$ due to molecules with inactive acceptor dye (gray shading). (*B*) 2D histogram of relative donor fluorescence lifetime versus *E*. τ_{DA} is the donor lifetime in the presence of the acceptor, τ_D in the absence of acceptor. The straight line shows the dependence for a fixed distance, the curved lines the dependences for a Gaussian chain (solid) and a worm-like chain (dashed). (*C–E*) nsFCS measurements reporting on donor-acceptor distance dynamics in unfolded Csp at 1.7 M GdmCl. A global fit of donor-donor (*C*), acceptor-acceptor (*D*), and donor-acceptor correlations (*E*) is used to determine the reconfiguration time τ_r that characterizes the dynamics in the unfolded state (21, 42, 44). The autocorrelation functions (*C*, *D*) exhibit the correlated, and the crosscorrelation function (*E*) the anticorrelated behavior expected for distance dynamics (43) on the timescale of approximately 100 ns. The much faster anticorrelated signal in the range of a few nanoseconds (photon antibunching) is due to the intrinsic photophysical kinetics of the FRET process (21, 43).

Probing Internal Friction by Solvent Viscosity Variation. The most common and model-independent way of quantifying solvent-independent internal friction is a variation of solvent viscosity, η, and extrapolation to $\eta = 0$ (26). This approach has previously been used for investigating internal friction in native proteins (1) and at the transition state; i.e., for assessing the influence of internal friction on folding kinetics (9, 15, 23, 34, 35); here, we extend it to unfolded proteins. Fig. 2 shows the reconfiguration times τ_r of terminally labeled unfolded Csp at different guanidinium chloride (GdmCl) concentrations as a function of η, adjusted by varying the concentration of glycerol. Over the range of η used here, the glycerol concentration has no significant effect on the transfer efficiencies of the unfolded state subpopulations, which indicates that the equilibrium distributions and thus the energetics of the system are largely unaffected by the viscogen (Fig. S2). In all cases, the solvent viscosity dependences of τ_r are well described by linear relations. In the absence of solvent-independent internal friction, we expect τ_r to approach zero upon extrapolation to zero solvent viscosity, a behavior we indeed observe in 6 M GdmCl. In viscosity-dependent measurements at lower GdmCl concentrations, however, the values of τ_r extrapolated to $\eta = 0$ are greater than zero, suggesting a contribution from a solvent viscosity-independent timescale due to internal friction, τ_i, in addition to a solvent viscosity-dependent timescale equivalent to the reconfiguration time in the absence of internal friction, τ_s.

A framework for interpreting this result is provided by theories of polymer dynamics, where the additivity of τ_i and τ_s is well established (14, 26, 45, 46). Such additivity can be rigorously justified in an extension of the Rouse model known as the Rouse model with internal friction (RIF), which leads to an additional characteristic timescale, τ_i, associated with internal friction. The mathematical structure of the RIF model (see *Supporting Information*, Eq. S3 ff.) is such that the spatial dependences of the relaxation modes of the chain are identical to those of the Rouse modes while each corresponding relaxation time, $\tau^{(n)}$, is increased by the same amount τ_i; i.e.,

$$\tau^{(n)} = \tau_{\mathrm{Rouse}}/n^2 + \tau_i, \qquad n = 1, 2, \ldots \qquad [1]$$

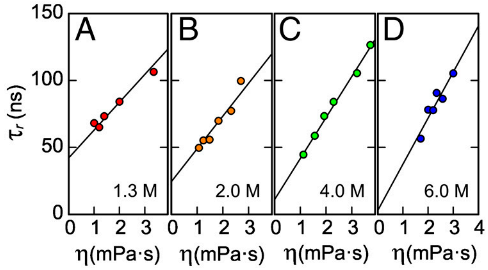

Fig. 2. Solvent viscosity (η) dependences of chain reconfiguration times of terminally labeled Csp at different GdmCl concentrations (indicated in the lower right of each panel). Based on Eq. 2, data were fit with $(\tau_r)_{\mathrm{GdmCl}} = a \cdot \langle r^2 \rangle_{\mathrm{GdmCl}} \eta/\eta_0 + (\tau_i)_{\mathrm{GdmCl}}$ (solid lines, see *Supporting Information*), where the mean-squared end-to-end distances at a given GdmCl concentration, $\langle r^2 \rangle_{\mathrm{GdmCl}}$, are obtained from corresponding FRET efficiency histograms. *a* is a global fit parameter for all GdmCl concentrations, and the values of the internal friction time, $(\tau_i)_{\mathrm{GdmCl}}$, correspond to the intercepts.

---

*We used here a variant of Csp devoid of Trp residues (see *Supporting Information* for details). A comparison to previous results (21, 37) shows that the collapse behavior and the dynamics of the chain are not affected significantly by this modification.

Here, $\tau_{\mathrm{Rouse}} = \langle r^2\rangle/(3\pi^2 D_t(\eta))$ is the largest relaxation time of the Rouse chain (25); $\langle r^2\rangle$ is the mean squared end-to-end distance of the chain; $D_t(\eta)$ is the solvent viscosity-dependent translational diffusion coefficient of the chain with $D_t \sim \eta^{-1}$; and n is the mode number. The overall solvent-dependent relaxation time, τ_s, is the same as τ_{Rouse} to within a numerical factor (47), leading to the same dependence on solvent viscosity, η, and chain dimension:

$$\tau_s \propto \langle r^2\rangle\eta. \qquad [2]$$

The common assumption that only the dynamics corresponding to τ_s depend on solvent viscosity, and τ_i does not (26), thus leads to the relation

$$\tau_r = \tau_i + \frac{\eta}{\eta_0}\tau_s(\eta_0), \qquad [3]$$

where η_0 is the viscosity of water.[†] τ_i thus corresponds to the extrapolated value of τ_r at $\eta = 0$ (Fig. 2). From a global fit of the datasets at all denaturant concentrations (*Supporting Information*), we find that τ_i increases with decreasing GdmCl concentration from a value indistinguishable from zero within experimental uncertainty at 6.0 M GdmCl (3±4 ns) to 19 ±2 ns, 28±2 ns, and 40±2 ns at 4.0 M, 2.0 M, and 1.3 M GdmCl, respectively. At the highest denaturant concentrations, the chains are thus sufficiently expanded that internal friction is negligible [‡], but at lower denaturant concentrations, where the chains are more compact (29, 37, 38), a large part of the reconfiguration time is due to internal friction. To exclude possible viscogen-specific effects or uncertainties in the type of function used for extrapolation (34), we combine our results with an independent approach.

Probing Internal Friction by Segment Length Variation. A complementary way of assessing the role of internal friction that does not rely on a change in solvent viscosity is the analysis of the reconfiguration times for different segments of the chain as probed by different labeling positions. Since a polymer exhibits a spectrum of fluctuation timescales or relaxation modes, each associated with a different length scale, segments of different lengths probe different parts of this spectrum (47, 48). As a result, the *relative* influence of internal friction on the reconfiguration dynamics will depend on the length of the segments (45). We thus prepared variants of Csp with the FRET labels in different positions (Table S1) and determined the reconfiguration times at different GdmCl concentrations (Fig. 3).[§] Interestingly, at different GdmCl concentrations, the relative reconfiguration times (normalized by τ_r of the terminally labeled chain) exhibit very different dependences on the segment length. At 7 M GdmCl, the increase in τ_r from the shortest to the longest segment is pronounced, in agreement with both theory and simulations of polymers without internal friction (47). However, τ_r becomes less dependent on segment length with decreasing GdmCl concentration. Qualitatively, this is expected if internal friction dominates chain dynamics: in the limit where $\tau_i \gg \tau_{\mathrm{Rouse}}$, Eq. **1** suggests that all modes will approach the same relaxation time τ_i, and τ_r will become independent of the segment length probed.

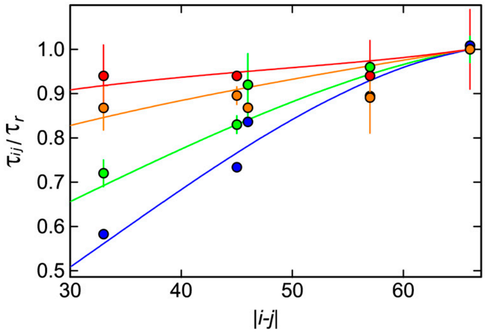

Fig. 3. Dependence of chain dynamics on the length of the polypeptide segment probed (Table S1) in unfolded Csp at different GdmCl concentrations (1.3 M: red, 2.0 M: orange, 4.0 M: green, 7.0 M: blue). Error bars represent standard deviations estimated from independent measurements where available. The reconfiguration time, τ_{ij}, for donor and acceptor in positions i and j normalized by the end-to-end reconfiguration time, τ_r, is shown as a function of the segment length, $|i-j|$. The fits with the modified RIF model (*Supporting Information*) used to determine the characteristic timescale associated with internal friction, τ_i, are shown as solid lines.

It was previously shown that a simple Rouse model agrees remarkably well with coarse-grained simulations of polypeptide dynamics that take into account both excluded volume and hydrodynamic interactions (47). We thus expect that the RIF model is similarly adequate when applied to situations where internal friction effects are important. To analyze our experimental results quantitatively, it was necessary to extend the RIF model (see *Supporting Information*). Specifically, the observed compaction of unfolded Csp with decreasing denaturant concentration (29, 37, 38) (Fig. S3) was mimicked by including a weak harmonic constraining potential adjusted to reproduce the experimentally determined value of $\langle r^2\rangle$ for the unfolded protein at the respective GdmCl concentrations (for comparison with coarse-grained simulations see Fig. S4). The effect of internal friction was included as an additional timescale τ_i that is independent of the chain segment probed (Eq. **1**), but can vary with changes in $\langle r^2\rangle$. Finally, the FRET dyes were taken into account explicitly and modeled as additional beads connected to the rest of the chain via harmonic springs [¶].

This model allows us to quantify the contribution of internal friction by adjusting τ_i for each GdmCl concentration such that the calculated reconfiguration times as a function of the segment length fit the experimental data (*Supporting Information*). Fig. 3 shows the good agreement of theory and experiment. The data measured in 7 M GdmCl are well fit by the Rouse model in the absence of internal friction. For 4 M, 2 M, and 1.3 M GdmCl, the resulting values for τ_i are 9±3 ns, 22±6 ns, and 30(+30,−20) ns, respectively, in good agreement with the results obtained from the solvent viscosity-dependent measurements (Fig. 2). This agreement suggests that a linear extrapolation of τ_r to $\eta = 0$ is a good approximation, and it lends additional support to the additivity of timescales as suggested in Eq. **3** [‖]. However, these results are limited to GdmCl concentrations above approximately 0.8 M, where the population and thus the signal contribution of the unfolded state are large enough to allow measurements at equilibrium.

Probing Internal Friction by Denaturant Variation and Microfluidic Mixing. To enable a determination of τ_r in the virtual absence of

---

[†] Note that even though we are not aware of a model that accounts for internal friction within the Zimm framework, given the same linear dependence of the Zimm time on solvent viscosity (25), it is plausible to assume that the effect of internal friction is also additive and described by Eq. **3**.

[‡] We note that residual structure in unfolded proteins detected by NMR has usually been observed in a range of urea concentrations that corresponds to up to approximately 4 M of the stronger denaturant GdmCl (28), where we still observe a significant contribution of internal friction. A direct comparison to such measurements may help to identify the molecular origin of internal friction.

[§] Note that we used here a variant of Csp devoid of Trp residues to eliminate the influence of static quenching on the correlation functions (see *Supporting Information*).

[¶] Note that all parameters in the extended RIF model are either well constrained by experimental observables or have insignificant effects on the overall results when varied within reasonable bounds (see *Supporting Information*), such that τ_i is the only free fit parameter.

[‖] A purely multiplicative effect of internal friction on reconfiguration times (16) would not affect the ratios of times plotted in Fig. 3 and would thus be not sufficient to explain the experimental results.

denaturant, where the unfolded state is most compact (21, 29, 37) and where the effect of internal friction is expected to be most pronounced, we use a microfluidic mixing device that has recently been developed for investigating rapid protein folding reactions with single-molecule fluorescence (49, 50). By mixing protein unfolded in 1.5 M GdmCl entering from the middle inlet channel with denaturant-free buffer entering via the side channels (Fig. 4*B*) at a volume ratio of 1∶7, we can populate the unfolded state transiently with a dead time of approximately 5 ms (49). Under our experimental conditions, the folding time of Csp is in the range of 10 ms (38), which allows us to probe the dynamics of unfolded protein at 0.2 M GdmCl with nsFCS measurements in the early part of the observation channel, where the majority of the protein is still unfolded (Fig. 4*C*). We obtain a value for τ_r of 115 ns under these near-native conditions (Fig. 4).

Fig. 4 shows the measured values of τ_r for unfolded Csp over the entire range of GdmCl concentrations accessible. A clear increase in τ_r with decreasing GdmCl concentrations is observed below approximately 2 M, indicating the onset of internal friction; at GdmCl concentrations above approximately 5 M, τ_r increases due to the increasing viscosity of the denaturant solution. Our results in Figs. 2 and 3 indicate that internal friction is absent above 6 M GdmCl. We can thus equate τ_r and τ_s under these conditions (Eq. **3**) and use the scaling behavior expected from polymer dynamics ($\tau_s \propto \langle r^2 \rangle \eta$ for the Rouse model, Eq. **2**) to obtain τ_s at all GdmCl concentrations. With the values of $\langle r^2 \rangle$ determined from the FRET efficiencies (Fig. S3) and the measured solvent viscosities, we can thus obtain the GdmCl concentration dependence of τ_s (Fig. 4, solid gray line). The differences between the observed values of τ_r and the calculated values of τ_s then yield the internal friction times τ_i (Eq. **3**, Fig. 4*A*)**. Remarkably, the resulting dependence of τ_i on GdmCl concentration agrees well both with the values from the solvent viscosity-dependent measurements (Fig. 2) and the analysis based on the different segment lengths (Fig. 3). This agreement illustrates the consistency of the three different approaches we used to quantify internal friction, and it suggests that the result is robust and model-independent.

In summary, we can thus quantify the contribution of internal friction to the dynamics of unfolded Csp under solution conditions ranging from the virtual absence of denaturant to more than 7 M GdmCl. At the highest denaturant concentrations, the chains appear to be sufficiently expanded that internal friction becomes negligible, but in the absence of denaturant, where the chains are most compact, internal friction dominates the reconfiguration time, with a value of τ_i that is about an order of magnitude greater than τ_s.

Internal Friction in IDPs: Role of Sequence Composition. To investigate how internal friction depends on amino acid composition, we studied the dynamics of two IDPs, the N-terminal domain of HIV integrase (IN), and the C-terminal segment of human prothymosin α (ProTα), which contain a larger fraction of charged and hydrophilic amino acids than Csp. The dimensions of IDPs have previously been shown to be modulated strongly by the interactions of charged residues within the chain (41, 51), and both IN and ProTα exhibit an expansion due to charge repulsion at low ionic strength (41) (Fig. S3). Here, IN was investigated in the absence of its ligand Zn^{2+}, so both IDPs are disordered even in the absence of denaturant (41), and their unfolded state dynamics can be investigated at equilibrium over the entire range of GdmCl concentrations.

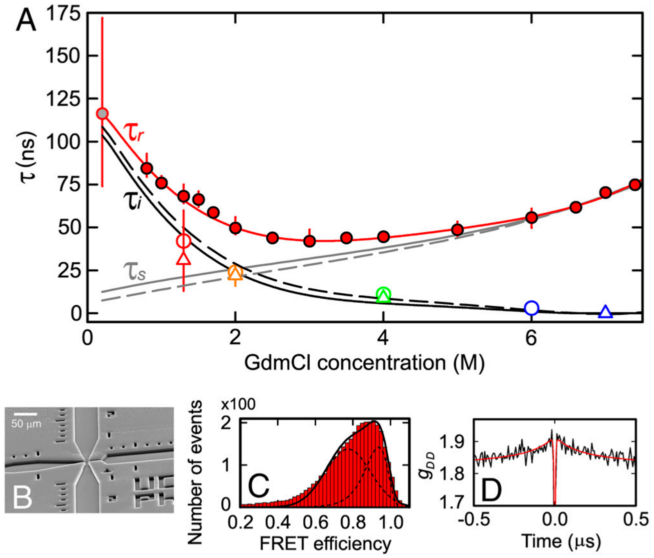

Fig. 4. Quantifying internal friction in unfolded Csp as a function of denaturant concentration. (*A*) The experimentally determined GdmCl dependence of the end-to-end reconfiguration time, τ_r, obtained in equilibrium measurements (filled red circles) and from microfluidic mixing (gray filled circle), with an empirical polynomial fit used for interpolation (red line). The solid (dashed) gray line shows the reconfiguration time expected for a Rouse (Zimm) chain in the absence of internal friction, τ_s (see main text). τ_i, the characteristic timescale associated with internal friction, calculated according to Eq. **3**, is shown as a solid (dashed) black line for the Rouse (Zimm) model. The values of τ_i from Figs. 2 and 3 are shown as open circles and triangles, respectively, for comparison. (*B*) Electron micrograph of the microfluidic mixer used to determine τ_r in the absence of denaturant. FRET efficiency histogram (*C*) and donor-donor nsFCS curve (*D*) acquired (8 ± 2) ms after mixing. The uncertainties of τ_r were estimated by bootstrapping.

At high GdmCl concentrations, both the dimensions (Fig. S3) (41) and the reconfiguration times (Fig. 5) of IN, ProTα, and terminally labeled Csp converge, as expected for polypeptide segments of similar length under conditions where charge interactions are shielded by the ionic denaturant, and where proteins follow the length scaling expected for simple homopolymers (52). At lower GdmCl concentrations, however, the dynamics of the three proteins clearly diverge. Below 2 M GdmCl, IN shows an increase in τ_r, but to a lesser extent than Csp. Remarkably, τ_r of ProTα is almost independent of GdmCl concentration. With the

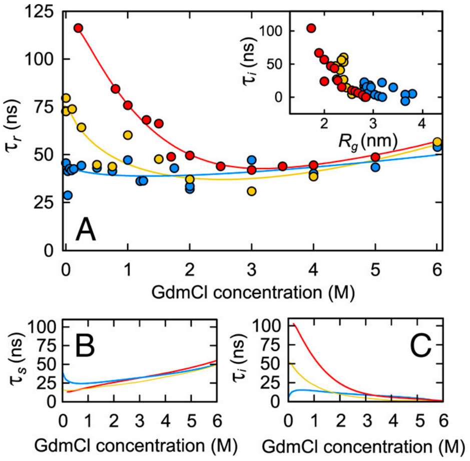

Fig. 5. Comparison of internal friction in Csp and IDPs. (*A*) Measured reconfiguration times of Csp (red circles), integrase (yellow circles), and ProTα (blue circles) as a function of GdmCl concentration. Polynomial fits used for interpolation are shown as solid lines. Reconfiguration time expected for a Rouse chain, τ_s, (*B*) and internal friction times, τ_i, (*C*) calculated from (A) as in Fig. 4. (*Inset* in *A*) Dependence of τ_i on the radius of gyration, R_g, for Csp (red), integrase (yellow), and ProTα (blue) for all conditions in (*A*).

**The corresponding analysis with the Zimm model, where τ_s is scaled by $\langle r^2 \rangle^{3/2}$ (25), yields very similar results (Fig. 4), indicating that the procedure is robust with respect to the polymer model used.

procedure analogous to the one used for Csp (Fig. 4, Eq. **3**) to separate τ_r into contributions of τ_s and τ_i, we find a similar dependence of τ_s for the three proteins, but very different contributions of internal friction (Fig. 5 *B* and *C*). The values of τ_s differ significantly only at the lowest GdmCl concentrations, where charge repulsion sets in (Fig. S3); especially ProTα shows a slight increase in τ_s concomitant with its expansion (41) (Fig. S3; Eq. **2**).

The contribution of internal friction appears to be strongly dependent on the dimensions of the chain (Fig. 5*C*). IN exhibits a value of τ_i at 0 M GdmCl of about half the value of Csp, accompanied by a significantly less pronounced collapse (Fig. S3). Internal friction in ProTα remains low throughout and shows an additional drop below 1 M GdmCl, where the pronounced charge-mediated chain expansion sets in (41) (Fig. S3). The observation for ProTα that adding 1 M KCl in the absence of GdmCl also results in collapse (41) and an increase in τ_i (Fig. S5*A*) confirms that charge interactions (and not denaturant-specific interactions) are the dominant cause of this effect. The dependence of internal friction on chain dimensions is further illustrated by an inverse correlation of τ_i with R_g when all proteins and solution conditions are taken together (Fig. 5*A*, *Inset*). Internal friction in unfolded proteins thus decreases not only with increasing concentrations of denaturant, but also with increasing repulsive charge interactions in the chain, both of which lead to an expansion of the polypeptide.

Discussion

Timescale of Unfolded State Dynamics. The results presented here, together with previous work (21, 32, 40, 42, 53), show that the relaxation dynamics of unfolded proteins in the absence of pronounced residual structure occur on timescales in the range expected for simple polymers based on theoretical concepts such as Rouse or Zimm theory (25). These diffusive dynamics put a limit on the timescale of forming long-range interactions within the chain, and are thus closely related to the effective diffusion coefficient on a free energy surface that can be used to describe the folding process in terms of Kramers-type theories (10, 21, 22) [††]. Similar timescales have also been observed for unfolded state dynamics in molecular simulations (40, 58), and the same timescales are expected to govern the initial collapse of the chain from a more extended conformation (21). In the case of small cold shock proteins, previous experiments suggest that dynamics above the 100 ns range and below the millisecond timescale of folding are absent (42, 59). Such a separation of the timescales of unfolded state dynamics on the one hand and of barrier crossing on the other is a characteristic of systems well approximated by two-state kinetics (60). In contrast, for proteins folding in microseconds, the 100 ns timescale is sufficiently close to the barrier crossing times that changes in unfolded state dynamics need to be taken into account for a description of their rapid folding dynamics (22).

Mechanisms of Internal Friction. Even though the concept that polymer chains are subject to internal friction has been well established in the field of polymer dynamics for more than half a century (14, 26, 45, 46), the molecular origin of internal friction has largely remained elusive. In terms of the kinetic description, at least two cases of internal friction can be distinguished. In one case, internal friction results in a change of the effective viscosity, η_{eff}, that will affect the dynamics in a purely multiplicative way; e.g., $\tau = \tau_0 \eta_{\mathrm{eff}}/\eta$, with $\eta_{\mathrm{eff}} = \eta \exp(\varepsilon/k_{\mathrm{B}}T)^2$, where τ is the observed relaxation time of the process (e.g. chain reconfiguration); τ_0 is the relaxation time in the absence of internal friction; ε is the mean energetic roughness causing internal friction; k_{B} is Boltzmann's constant; and T is temperature (16). This type of behavior would entail that the relaxation time approaches zero upon extrapolation to $\eta = 0$; it would also imply full solvation of all parts of the macromolecule involved in internal friction processes ("wet" friction). In the other case, internal friction results in a constant timescale that is additive with the intrinsic dynamic timescale of the process in the absence of internal friction (14, 26, 45, 46). This behavior is suggestive of the exclusion of solvent from those parts of the polypeptide whose interactions cause internal friction (1), corresponding to "dry" friction. In our experiments, the extrapolation to zero solvent viscosity (Fig. 2), the position dependence of the reconfiguration times (Fig. 3), and the lack of a dependence of τ_i on solvent viscosity (Fig. 2 and consistency with Figs. 3 and 4) are unexpected for a multiplicative effect and clearly favor the additive contribution of an internal friction time (Eqs. **1**, **3**); i.e., "dry" friction.

A clue regarding the molecular contributions comes from the denaturant dependence of τ_r (Fig. 4): since dihedral angle rotations may not be expected to be accelerated by denaturant binding, but side chain or backbone interactions will be weakened, the latter may be the more probable cause of internal friction in our unfolded proteins, an inference that is supported by recent simulations (8). The similarity of the degree of unfolded state collapse for different chain segments (37) (Fig. S6) and the good agreement of the position dependence of the dynamics with a model that ignores specific sequence effects (Fig. 3) indicate that specific long-range interactions (e.g., clustering of hydrophobic residues distant in sequence) do not play a dominant role here. Furthermore, simulations show that specific interactions between two points along the chain cannot reproduce the position dependence of the dynamics we observe (Fig. S7), suggesting the predominance of nonspecific interactions evenly distributed along the chain. The prevalence of interactions that are short-range in sequence is also supported by the dynamics of a bisected variant of Csp, whose internal friction times are very similar to those of the full-length protein (Fig. S8).

A surprisingly large reconfiguration time of approximately 20 μs was recently suggested for compact unfolded protein L based on tryptophan triplet state quenching experiments (33). In spite of the large contribution of internal friction that would have to be invoked to explain this result, the contact formation rate extrapolated to $\eta = 0$ was indistinguishable from zero within experimental error. This observation would demand a dominant contribution of "wet" friction; i.e., complete solvation of the groups whose interactions cause internal friction, in contrast to our observations on the proteins investigated here. The uncertainty in the intercept of the solvent viscosity dependence of the contact rates of Waldauer et al. (33) does leave room for a possible contribution of "dry" friction in protein L, but this effect might be difficult to distinguish from a reaction-limited component of the quenching process. Contact formation experiments with a diffusion-limited quencher may help to address this question further. Results based on the almost diffusion-limited quenching of an oxazine dye by tryptophan in a 26 residue segment within the small binding domain BBL resulted in timescales of internal contact formation extrapolated to zero solvent viscosity of approximately 0.3 μs (61), comparable to the timescales due to internal friction observed here. A direct combination of FRET and contact quenching experiments may allow the identification of possible differences in internal friction between compact and expanded conformations within the ensemble of unfolded proteins.

Even though the detailed molecular origin of internal friction is still unclear, the approach to quantify internal friction developed here now opens the possibility of a more systematic investigation, aided, e.g., by a quantitative comparison with atomistic simulations or polymer models (14, 45, 47, 62). Approaches such

---

[††] Note that contact formation probed in quenching experiments (54, 55) for similar sequence separations is expected to occur on longer timescales than in FRET experiments (typically in the microsecond range) because of the low probability of populating sufficiently small intramolecular distances in the corresponding equilibrium distance distributions [see, e.g., (56, 57)].

as the molecular transfer model (31) may facilitate the inclusion of the effects of denaturants or other cosolvents.

Effect of Internal Friction on the Dynamics of Protein Folding and IDPs. What do our results imply for the influence of internal friction on protein folding kinetics? For this question, it would be of interest to determine the effect of internal friction on chain dynamics for unstructured conformational ensembles that are as compact as the transition state. Based on the correlation of τ_i with R_g (Fig. 5), we can estimate the magnitude of τ_i in this compact regime. The transition state for folding of Csp exhibits native-like solvent accessibility (63), so we assume R_g of the native state (1.3 nm) as a lower bound on the dimensions of the transition state and estimate an extrapolated value of $\tau_i \approx (0.3 \pm 0.1)$ μs. A contribution of internal friction of this magnitude to the millisecond folding time of Csp is too small to be detectable experimentally (2, 15), but ultrafast-folding proteins exhibit contributions of internal friction ranging from approximately 0.7 μs to several microseconds (9, 15, 35). This observation suggests that for microsecond folders a contribution of τ_i in the range of 0.3 μs can have a significant effect on their folding rates (22), but the remaining discrepancy implies the existence of additional contributions or a change in mechanism of internal friction in the barrier region. The latter may not be entirely unexpected given the importance of the specific interactions in transition state ensembles. The mechanisms and the extent of internal friction at the transition state will depend on the relevant length scales and the possible role of collective modes that characterize the conformational transitions involved in the barrier crossing process (64). The importance of specific interactions for energetic roughness has recently been proposed for the folding of spectrin domains (23), which may allow a quantitative assessment of such effects.

The role of internal friction for the conformational dynamics of proteins is not limited to the folding reaction. With the realization that intrinsic disorder is an important property of a large number of proteins involved in intracellular interactions and regulatory processes (27, 28), the ability to quantify internal friction and to elucidate the underlying mechanisms will be crucial for understanding the properties of IDPs. Our observation that the contribution of internal friction depends on amino acid composition and charge repulsion (Fig. 5) may have important implications for the dynamics of intermolecular interactions involving IDPs. In a "flycasting" mechanism of the interactions of IDPs with a cellular target (65), both an increase in chain dimensions (41, 51) and higher reconfiguration rates of an IDP may contribute to an increase in the rate of binding.

Methods

Proteins were expressed, purified, and labeled with Alexa 488 and Alexa 594 essentially as reported previously (37, 41, 42). Single-molecule measurements were performed using a Micro Time 200 confocal microscope equipped with a HydraHarp 400 counting module (PicoQuant). For rapid mixing experiments, microfluidic mixers fabricated by replica molding in PDMS were used (49, 50). For details on experiments, theory, and simulations, see *Supporting Information*.

ACKNOWLEDGMENTS. We thank Dr. J. Clark, I. König, and R. Wuttke for help in protein preparation, and Drs. A. Borgia, W. Eaton, H. Hofmann, L. Lapidus, R. Netz, and D. Thirumalai for helpful discussions. This work was supported by the Swiss National Science Foundation (to B.S.), the NCCR for Structural Biology (to B.S.), a Starting Investigator Grant of the European Research Council (to B.S.), the National Science Foundation (Grants CHE 0848571 and PHY05-51164, to D.E.M.), and the Robert A. Welch Foundation (grant F-1514, to D.E.M.).

1. Ansari A, Jones CM, Henry ER, Hofrichter J, Eaton WA (1992) The role of solvent viscosity in the dynamics of protein conformational changes. *Science* 256:1796–1798.
2. Jacob M, Geeves M, Holtermann G, Schmid FX (1999) Diffusional barrier crossing in a two-state protein folding reaction. *Nat Struct Biol* 6:923–926.
3. Plaxco KW, Baker D (1998) Limited internal friction in the rate-limiting step of a two-state protein folding reaction. *Proc Natl Acad Sci USA* 95:13591–13596.
4. Ladurner AG, Fersht AR (1999) Upper limit of the time scale for diffusion and chain collapse in chymotrypsin inhibitor 2. *Nat Struct Biol* 6:28–31.
5. Bryngelson JD, Onuchic JN, Socci ND, Wolynes PG (1995) Funnels, pathways, and the energy landscape of protein folding: a synthesis. *Proteins* 21:167–195.
6. Socci ND, Onuchic JN, Wolynes PG (1996) Diffusive dynamics of the reaction coordinate for protein folding funnels. *J Chem Phys* 104:5860–5868.
7. Krivov SV, Karplus M (2008) Diffusive reaction dynamics on invariant free energy profiles. *Proc Natl Acad Sci USA* 105:13841–13846.
8. Best RB, Hummer G (2010) Coordinate-dependent diffusion in protein folding. *Proc Natl Acad Sci USA* 107:1088–1093.
9. Cellmer T, Henry ER, Hofrichter J, Eaton WA (2008) Measuring internal friction of an ultrafast-folding protein. *Proc Natl Acad Sci USA* 105:18320–18325.
10. Best RB, Hummer G (2011) Diffusion models of protein folding. *Phys Chem Chem Phys* 13:16902–16911.
11. Liu F, Nakaema M, Gruebele M (2009) The transition state transit time of WW domain folding is controlled by energy landscape roughness. *J Chem Phys* 131:195101.
12. Chahine J, Oliveira RJ, Leite VBP, Wang J (2007) Configuration-dependent diffusion can shift the kinetic transition state and barrier height of protein folding. *Proc Natl Acad Sci USA* 104:14646–14651.
13. Kramers HA (1940) Brownian motion in a field of force and the diffusion model of chemical reactions. *Physica* 7:284–304.
14. Portman JJ, Takada S, Wolynes PG (2001) Microscopic theory of protein folding rates. II. Local reaction coordinates and chain dynamics. *J Chem Phys* 114:5082–5096.
15. Hagen SJ (2010) Solvent viscosity and friction in protein folding dynamics. *Curr Protein Pept Sci* 11:385–395.
16. Zwanzig R (1988) Diffusion in a rough potential. *Proc Natl Acad Sci USA* 85:2029–2030.
17. Hyeon CB, Thirumalai D (2003) Can energy landscape roughness of proteins and RNA be measured by using mechanical unfolding experiments? *Proc Natl Acad Sci USA* 100:10249–10253.
18. Whitford PC, et al. (2010) The origin of nonmonotonic complex behavior and the effects of nonnative interactions on the diffusive properties of protein folding. *Biophys J* 99:600–608.
19. Alexander-Katz A, Wada H, Netz RR (2009) Internal friction and nonequilibrium unfolding of polymeric globules. *Phys Rev Lett* 103:028102.
20. Wang J, Oliveira RJ, Whitford PC, Chahine J, Leite VBP (2010) Coordinate and time-dependent diffusion dynamics in protein folding. *Methods* 52:91–98.
21. Nettels D, Gopich IV, Hoffmann A, Schuler B (2007) Ultrafast dynamics of protein collapse from single-molecule photon statistics. *Proc Natl Acad Sci USA* 104:2655–2660.
22. Cellmer T, Henry ER, Kubelka J, Hofrichter J, Eaton WA (2007) Relaxation rate for an ultrafast folding protein is independent of chemical denaturant concentration. *J Am Chem Soc* 129:14564–14565.
23. Wensley BG, et al. (2010) Experimental evidence for a frustrated energy landscape in a three-helix-bundle protein family. *Nature* 463:685–U122.
24. Kubelka J, Hofrichter J, Eaton WA (2004) The protein folding 'speed limit'. *Curr Opin Struct Biol* 14:76–88.
25. Doi M, Edwards SF (1988) *The Theory of Polymer Dynamics* (Oxford UniversityPress, USA New York).
26. De Gennes PG (1979) *Scaling Concepts in Polymer Physics* (Cornell University Press, Ithaca, NY).
27. Dunker AK, Silman I, Uversky VN, Sussman JL (2008) Function and structure of inherently disordered proteins. *Curr Opin Struct Biol* 18:756–764.
28. Dyson HJ, Wright PE (2004) Unfolded proteins and protein folding studied by NMR. *Chem Rev* 104:3607–3622.
29. Schuler B, Eaton WA (2008) Protein folding studied by single-molecule FRET. *Curr Opin Struct Biol* 18:16–26.
30. Ziv G, Thirumalai D, Haran G (2009) Collapse transition in proteins. *Phys Chem Chem Phys* 11:83–93.
31. O'Brien EP, Ziv G, Haran G, Brooks BR, Thirumalai D (2008) Effects of denaturants and osmolytes on proteins are accurately predicted by the molecular transfer model. *Proc Natl Acad Sci USA* 105:13403–13408.
32. Möglich A, Joder K, Kiefhaber T (2006) End-to-end distance distributions and intrachain diffusion constants in unfolded polypeptide chains indicate intramolecular hydrogen bond formation. *Proc Natl Acad Sci USA* 103:12394–12399.
33. Waldauer SA, Bakajin O, Lapidus LJ (2010) Extremely slow intramolecular diffusion in unfolded protein L. *Proc Natl Acad Sci USA* 107:13713–13717.
34. Jas GS, Eaton WA, Hofrichter J (2001) Effect of viscosity on the kinetics of alpha-helix and beta- hairpin formation. *J Phys Chem B* 105:261–272.
35. Qiu LL, Hagen SJ (2004) A limiting speed for protein folding at low solvent viscosity. *J Am Chem Soc* 126:3398–3399.
36. Sherman E, Haran G (2011) Fluorescence correlation spectroscopy of fast chain dynamics within denatured protein L. *Chemphyschem* 12:696–703.
37. Hoffmann A, et al. (2007) Mapping protein collapse with single-molecule fluorescence and kinetic synchrotron radiation circular dichroism spectroscopy. *Proc Natl Acad Sci USA* 104:105–110.
38. Schuler B, Lipman EA, Eaton WA (2002) Probing the free-energy surface for protein folding with single-molecule fluorescence spectroscopy. *Nature* 419:743–747.
39. Sherman E, Haran G (2006) Coil-globule transition in the denatured state of a small protein. *Proc Natl Acad Sci USA* 103:11539–11543.
40. Nettels D, et al. (2009) Single molecule spectroscopy of the temperature-induced collapse of unfolded proteins. *Proc Natl Acad Sci USA* 106:20740–20745.
41. Müller-Späth S, et al. (2010) Charge interactions can dominate the dimensions of intrinsically disordered proteins. *Proc Natl Acad Sci USA* 107:14609–14614.

42. Nettels D, Hoffmann A, Schuler B (2008) Unfolded protein and peptide dynamics investigated with single-molecule FRET and correlation spectroscopy from picoseconds to seconds. *J Phys Chem B* 112:6137–6146.
43. Wang ZS, Makarov DE (2003) Nanosecond dynamics of single polypeptide molecules revealed by photoemission statistics of fluorescence resonance energy transfer: A theoretical study. *J Phys Chem B* 107:5617–5622.
44. Gopich IV, Nettels D, Schuler B, Szabo A (2009) Protein dynamics from single-molecule fluorescence intensity correlation functions. *J Chem Phys* 131:095102.
45. Khatri BS, McLeish TCB (2007) Rouse model with internal friction: A coarse grained framework for single biopolymer dynamics. *Macromolecules* 40:6770–6777.
46. Manke CW, Williams MC (1985) Internal viscosity of polymers and the role of solvent resistance. *Macromolecules* 18:2045–2051.
47. Makarov DE (2010) Spatiotemporal correlations in denatured proteins: The dependence of fluorescence resonance energy transfer (FRET)-derived protein reconfiguration times on the location of the FRET probes. *J Chem Phys* 132:035104.
48. Cheng RR, Uzawa T, Plaxco KW, Makarov DE (2010) Universality in the timescales of internal loop formation in unfolded proteins and single-stranded oligonucleotides. *Biophys J* 99:3959–3968.
49. Pfeil SH, Wickersham CE, Hoffmann A, Lipman EA (2009) A microfluidic mixing system for single-molecule measurements. *Rev Sci Instrum* 80:055105.
50. Hofmann H, et al. (2010) Single-molecule spectroscopy of protein folding in a chaperonin cage. *Proc Natl Acad Sci USA* 107:11793–11798.
51. Mao AH, Crick SL, Vitalis A, Chicoine CL, Pappu RV (2010) Net charge per residue modulates conformational ensembles of intrinsically disordered proteins. *Proc Natl Acad Sci USA* 107:8183–8188.
52. Kohn JE, et al. (2004) Random-coil behavior and the dimensions of chemically unfolded proteins. *Proc Natl Acad Sci USA* 101:12491–12496.
53. Hillger F, et al. (2008) Probing protein-chaperone interactions with single molecule fluorescence spectroscopy. *Angew Chem Int Ed* 47:6184–6188.
54. Bieri O, et al. (1999) The speed limit for protein folding measured by triplet-triplet energy transfer. *Proc Natl Acad Sci USA* 96:9597–9601.
55. Lapidus LJ, Eaton WA, Hofrichter J (2000) Measuring the rate of intramolecular contact formation in polypeptides. *Proc Natl Acad Sci USA* 97:7220–7225.
56. Toan NM, Morrison G, Hyeon C, Thirumalai D (2008) Kinetics of loop formation in polymer chains. *J Phys Chem B* 112:6094–6106.
57. Cheng RR, Uzawa T, Plaxco KW, Makarov DE (2009) The rate of intramolecular loop formation in DNA and polypeptides: the absence of the diffusion-controlled limit and fractional power-law viscosity dependence. *J Phys Chem B* 113:14026–14034.
58. Lindorff-Larsen K, Piana S, Dror RO, Shaw DE (2011) How fast-folding proteins fold. *Science* 334:517–520.
59. Jacob M, et al. (1999) Microsecond folding of the cold shock protein measured by a pressure-jump technique. *Biochemistry* 38:2882–2891.
60. Zwanzig R (1997) Two-state models of protein folding kinetics. *Proc Natl Acad Sci USA* 94:148–150.
61. Neuweiler H, Johnson CM, Fersht AR (2009) Direct observation of ultrafast folding and denatured state dynamics in single protein molecules. *Proc Natl Acad Sci USA* 106:18569–18574.
62. Hyeon C, Morrison G, Thirumalai D (2008) Force-dependent hopping rates of RNA hairpins can be estimated from accurate measurement of the folding landscapes. *Proc Natl Acad Sci USA* 105:9604–9609.
63. Perl D, et al. (1998) Conservation of rapid two-state folding in mesophilic, thermophilic and hyperthermophilic cold shock proteins. *Nat Struct Biol* 5:229–235.
64. Straub JE, Sagnella DE, Thirumalai D (2000) Time scales and pathways for kinetic energy relaxation in solvated proteins: Application to carbonmonoxy myoglobin. *J Chem Phys* 113:7702–7711.
65. Shoemaker BA, Portman JJ, Wolynes PG (2000) Speeding molecular recognition by using the folding funnel: the fly-casting mechanism. *Proc Natl Acad Sci USA* 97:8868–8873.

Supporting Information

Soranno et al. 10.1073/pnas.1117368109

SI Text

SI Materials and methods. ***Protein preparation and labeling.*** Five different variants of Csp were prepared starting from a DNA sequence with an additional C-terminal cysteine (Table S1, CspC67). In contrast to the terminal positions, which are not influenced by quenching (1), previously published results on reconfiguration dynamics in the internal positions of Csp (2) were found to be affected by quenching of the FRET dyes by Trp side chains. Here we avoid this complication by replacing all Trp residues in the protein by Phe, which does not quench donor or acceptor (3). This lack of quenching is reflected by a more pronounced anticorrelation in the donor-acceptor cross-correlation functions (Fig. 1). The good agreement of the reconfiguration times obtained for the terminally labeled variant used here and the terminally labeled protein containing both Trp residues (1) (note that no fluorophore quenching is observed for the terminally labeled variant in both cases), indicates that the Trp to Phe exchanges do not affect unfolded state dynamics significantly. Several second cysteine residues were introduced by site-directed mutagenesis to provide specific labeling positions for the dyes (see Table S1 for all amino acid sequences). All variants were expressed with an N-terminal hexahistidine tag containing a tryptophan residue to facilitate detection and quantification by UV-Vis spectroscopy during purification. After purification, the proteins were digested with HRV 3C protease to cleave off the His-tag. The sequence CspC36C69 contains an additional protease cleavage site (Factor Xa) N-terminal to Cys36 for the preparation of a bisected variant that enables a comparison of the full length protein and the shortened peptide corresponding to the C-terminal segment alone. The synthetic starting gene (Celtek Bioscience) was cloned into vector pET47b (+). The variants were expressed in E. coli BL21 (DE3) and purified from the inclusion bodies using a HisTrap column (GE Healthcare, BioSciences AB) in 20 mM Tris-HCl, 0.5 M NaCl, 2 mM β-mercaptoethanol, 20 mM imidazole, 4 M GdmCl, pH 8.0 and elution with an imidazole gradient. The resulting protein was dialyzed against 50 mM sodium phosphate, 0.5 mM EDTA, 2 mM β-mercaptoethanol, pH 7.4 and digested by adding HRV 3C protease (containing a His-tag; 1mg HRV 3C per 55 mg Csp). Finally, digested Csp was separated from protease, uncleaved Csp, and free His-tag by a second HisTrap chromatography run. Labeling was performed as described previously (2, 4) and verified by mass spectrometry. IN and ProTα were expressed, purified, and labeled as described previously (5).

Single-molecule fluorescence spectroscopy. Single-molecule fluorescence measurements were performed with a MicroTime 200 confocal microscope (PicoQuant, Berlin, Germany) equipped with a diode laser (LDH-D-C-485, PicoQuant), a HeNe laser (594 nm, CWI Melles Griot) and an Olympus UplanApo 60x/1.20W objective (Olympus). Emitted photons were collected through the microscope objective, focused onto a 100 μm pinhole and then separated into four channels with a polarizing beam splitter and a dichroic mirror (585DCXR, Chroma). Photons emitted by the acceptor dye were additionally filtered (HQ650/100 Chroma Technology) and then focused onto a SPAD detector (Perkin Elmer). Photons emitted by the donor dye were filtered (ET525/50M, Chroma Technology) and detected with an avalanche photodiode (MPD, PDM series, 50 μm, PicoQuant). The arrival time of every detected photon was recorded by a HydraHarp 400 counting module (PicoQuant), and the time between excitation pulse and photon detection pulse was stored with 4 ps resolution (time resolution was thus limited by the timing jitter of the detectors).

The donor dye was excited with an average power of 100 μW. Single-molecule FRET efficiency histograms were acquired in samples with protein concentrations of about 20 pM to 50 pM; detected photons were recorded with a time resolution of 16 ps, with the laser in pulsed mode at a repetition rate of 64 MHz. Nanosecond-FCS measurements were performed in samples with a protein concentration of approximately 1 nM, with the laser in continuous wave mode, with typical data acquisition times of 10 to 16 h. Control measurements to determine the contribution of quenching to the acceptor intensity autocorrelation were carried out by exciting with a continuous wave HeNe laser (594 nm, CVI Melles Griot) at a power of 16 μW. All measurements were performed in 50 mM sodium phosphate buffer, pH 7.0, 150 mM β-mercaptoethanol, and 0.001% Tween 20 (Pierce) with varying concentrations of GdmCl. 20 mM cysteamine were added to enhance the fluorophore brightness and minimize bleaching.

Rapid mixing experiments were performed essentially as described by Hofmann et al. (6). Microfluidic mixers fabricated by replica molding in polydimethylsiloxane (PDMS) were used (6, 7). 200 pM of terminally labeled Csp unfolded in 1.5 M GdmCl from the inlet channel (from the left in Fig. 4*B*) were mixed with buffer without denaturant from the side channels (from the top and bottom in Fig. 4*B*), resulting in a final concentration of 0.25 M GdmCl in the observation channel (to the right in Fig. 4*B*). 0.015 % Tween 20 were included to prevent nonspecific interactions of the protein with the PDMS surfaces. Measurements were taken by placing the confocal volume at a position 50 μm (8 ms) downstream of the mixing region. The experiments were performed with pressures of 13.8 kPa (2.0 psi) applied to all channels. To estimate the time after mixing, the calculated average fully developed flow velocity of 1.2 mm/s (13.8 kPa) in the observation channel was corrected by accounting for the change in width of the observation channel from the mixing area to the observation point, as described by Pfeil et al. (7). The stability of the flow velocity during the measurements was confirmed by analyzing the donor-acceptor fluorescence intensity cross-correlation functions (8). nsFCS measurements were taken for 6 h and analyzed as described below (in *Nanosecond-FCS measurements*).

The viscosities of the solutions were measured with a digital viscometer (DV-I+, Brookfield Engineering) with a CP40 spindle and 30–60 rpm, which allows determination of viscosity with an uncertainty of 0.05 to 0.1 mPa s. The calibration of the instrument was tested with a reference solution of known viscosity. The changes in refractive index caused by the addition of viscogens and/or denaturant were determined with a digital Abbe refractometer (Krüss, Germany) and were taken into account for the calculation of the Förster radii for the corresponding solution conditions.

Data analysis. ***Fluorescence lifetimes and FRET efficiencies.*** The average fluorescence lifetimes were estimated as the mean detection time of the burst photons after donor excitation. The transfer efficiencies were obtained from $E = n_A/(n_A + n_D)$, where n_D and n_A are the numbers of donor and acceptor photons in the burst corrected for background, channel crosstalk, acceptor direct excitation, differences in quantum yields of the dyes, and detection efficiencies (9). For a fixed distance r, the mean donor lifetime in the presence of acceptor is given by $\tau_{DA} = \tau_{DA}(r) = \tau_D(1 - E(r))$, where τ_D is the lifetime in the absence of acceptor and $E(r) = 1/(1 + R_0^6/r^6)$, with the Förster radius R_0 calculated for the respective values of the refractive index of the solution (10) (black straight line in Fig. 1*B*). For a chain with a probability density function $P(r)$ of the interdye distance r, $\tau_{DA} = \int_0^\infty tI(t)\mathrm{d}t/\int_0^\infty I(t)\mathrm{d}t$ with $I(t) = I_0\int_0^\infty P(r)e^{-t/\tau_{DA}(r)}\mathrm{dr}$, where I is the time-dependent fluorescence emission intensity, and the mean FRET efficiency is calculated as $\langle E\rangle = \int_0^\infty E(r)P(r)\mathrm{dr}$. In Fig. 1*b*, a Gaussian chain distribution for the distances

$$P_{\mathrm{Gauss}}(r) = 4\pi r^2\left(\frac{3}{2\pi\langle r^2\rangle}\right)^{3/2}e^{-\frac{3r^2}{2\langle r^2\rangle}}, \qquad \textbf{[S1]}$$

(where $\langle r^2\rangle$ is the mean squared end-to-end distance of the segment probed) and the distribution of distances for a worm-like chain (11, 12) were compared. The resulting parametric plots are shown as the curved solid line (Gaussian chain) and the curved dashed line (worm-like chain), respectively. For the Gaussian chain, the corresponding radius of gyration, R_g, can be calculated from $R_g^2 = \langle r^2\rangle/6$. This conversion is used for the inset of Fig. 5 (main text) and for Figs. S2 and S6. For calculating persistence lengths, l_p, (Fig. S5), we use $l_p = \langle r^2\rangle/2l_c$, where l_c is the contour length of the segment probed (13), with corrections for dyes and linkers, as described previously (4). The insensitivity of the result to the detailed model used for the distance distribution is largely due to the similarity of the shape of the different distributions around their mean values given the low persistence lengths relative to the contour lengths of the polypeptides investigated here (5). Note that the long-range reconfiguration times observed here are much greater than the fluorescence lifetimes of the dyes; the effect of chain dynamics on the observed transfer efficiencies is thus negligible (14).

Nanosecond-FCS measurements. Autocorrelation curves of acceptor and donor channels and cross-correlation curves between acceptor and donor channels were calculated from measurements as described previously (1, 2). The data were fit over a time window of 4 μs with

$$g_{ij}(\tau) = 1 + \frac{1}{N}\left(1 - c_{\mathrm{AB}}e^{-\frac{t-t_0}{\tau_{\mathrm{AB}}}}\right)\left(1 + c_{\mathrm{CD}}e^{-\frac{t-t_0}{\tau_{\mathrm{CD}}}}\right)\left(1 + c_Te^{-\frac{t-t_0}{\tau_T}}\right),$$
$$i, j = A, D, \qquad \textbf{[S2]}$$

where N is the mean number of molecules in the confocal volume. The three multiplicative terms describe the contribution to amplitude and timescale of photon antibunching (AB), chain dynamics (CD), and triplet blinking of the dyes (T). In the case of the Csp variants, the three correlation curves were fit globally with the same values of τ_{CD} and t_0 above 1.5 M GdmCl. The amplitude and the lifetime of the antibunching and triplet component were fit with a free independent decay component for each correlation curve. Triplet lifetimes show a systematic increase in the range between 2 μs and 4 μs as the GdmCl concentration increases from 0 M to 7 M. Below 1.5 M GdmCl, only the donor autocorrelation was taken into account due to a significant contribution from the native state in the acceptor autocorrelation. The same approach was used for IN due to the presence of static quenching in the acceptor under native conditions. In the case of ProTα, data were fit globally over the entire range of GdmCl concentrations.

An estimation of the errors for Csp data has been obtained performing a Bootstrap-method, randomly sampling 50 subdatasets from the original dataset and fitting them with the same model. The obtained results have been used to estimate a standard deviation error from the mean. The resulting correlation times, τ_{CD}, can be described in terms of diffusion on the potential of mean force that corresponds to the $P(r)$ determined from the FRET efficiencies and fluorescence lifetimes and then converted in the reconfiguration time of the polypeptide chain (1).

Global fit of viscosity dependence of τ_r. The viscosity-dependent reconfiguration times measured at different GdmCl concentrations (Fig. 2) were fit globally according to Eq. **2** and **3** with $(\tau_r)_{\mathrm{GdmCl}} = a\cdot\langle r^2\rangle_{\mathrm{GdmCl}}\eta/\eta_0 + (\tau_i)_{\mathrm{GdmCl}}$, where $\langle r^2\rangle_{\mathrm{GdmCl}}$ is the mean square end-to-end distance of the chain as determined from single-molecule FRET experiments at a given GdmCl concentration, $(\tau_i)_{\mathrm{GdmCl}}$ is the "dry" internal friction contribution at the same GdmCl concentration, and a is a proportionality constant common to all GdmCl concentrations. According to the Rouse model, a can be related to the diffusion coefficient D_0 of a chain segment through $a = \frac{N}{3\pi^2D_0}$ (13). Assuming that N equals the number of Kuhn segments (including the contribution of dyes and linkers), we obtain a value of $D_0 = (0.73\pm0.03)\cdot10^{-5}$ cm^2/s, in a reasonable range for our segment size. The global fit describes the observed behavior at all the denaturant conditions well, as shown in Fig. 2, suggesting that if there is a contribution from "wet" friction, it would be the same irrespective of the solvent.

The viscosity dependences of the bisected variant of Csp at different GdmCl concentrations were fit globally as the data of the full length protein (Fig. S8). The global fit provides an estimate of the internal friction times, with 45 ± 4 ns, 29 ± 5 ns, and 12 ± 6 ns at 1.0 M, 2.0 M, and 6.0 M GdmCl, respectively. The proportionality constant a in the global fit was converted to diffusion coefficient of the elementary segment D_0 as explained for the full length variant. In this case, $D_0 = (0.7\pm0.2)\cdot10^{-5}$ cm^2/s, in excellent agreement with the value for the full length protein, suggesting that the model does not only provide the correct scaling with the mean squared end-to-end distance, but also the correct scaling with the length of the sequence.

Extended RIF model. The Rouse model with internal friction (RIF) assumes that a polymer chain obeys the following equations of motion:

$$-\xi_s\frac{d\mathbf{r}}{\mathrm{dt}} - \xi_i\mathbf{k}\frac{d\mathbf{r}}{\mathrm{dt}} - k_0\mathbf{kr} + \mathbf{f}(t) = 0 \qquad \textbf{[S3]}$$

Here $\mathbf{r}$ is the vector whose components are the positions of the polymer beads, k_0 is the stiffness of the spring connecting two adjacent beads, ξ_s and ξ_i are, respectively, the solvent- and the internal friction coefficients, $\mathbf{f}(t)$ is a random force vector satisfying the appropriate fluctuation-dissipation relationship, and $\mathbf{k}$ is a dimensionless connectivity matrix such that $k_0\mathbf{k}$ is the stiffness (Hessian) matrix of the chain. Specifically, this matrix is tridiagonal:

$$\mathbf{k} = \begin{bmatrix} -1 & 1 & 0 & 0 & \ldots \\ 1 & -2 & 1 & 0 & \ldots \\ 0 & 1 & -2 & 1 & \ldots \\ 0 & 0 & 1 & -2 & \ldots \\ \ldots & \ldots & \ldots & \ldots & \ldots \end{bmatrix}$$

These equations describe the Brownian dynamics of a linear chain of N beads with coordinates $\mathbf{r}_1, \mathbf{r}_2, \ldots, \mathbf{r}_N$, connected by harmonic springs such that the total potential energy is given by

$$V_0 = \frac{k_0}{2}\sum_{n=2}^{N}(\mathbf{r}_n - \mathbf{r}_{n-1})^2 \qquad \textbf{[S4]}$$

The mathematical structure of RIF is such that both the chain's stiffness matrix and the "friction matrix" $\xi_i\mathbf{k}$ appearing in the second term of Eq. **S3** are proportional to the same connectivity matrix. This results in a particularly simple eigenmode spectrum, where the presence of internal friction does not change the eigenmodes of the system (which remain identical to the Rouse modes), but shifts all of its characteristic times by a constant amount,

$$\tau^{(n)} = (\tau_{\mathrm{Rouse}}/n^2) + \tau_i, \qquad n = 1, 2, \ldots \qquad \textbf{[S5]}$$

where $\tau_i = \xi_i/k_0$ is the timescale associated with internal friction, and

$$\tau_{\mathrm{Rouse}} = \frac{\xi_s}{3\pi^2}\frac{N\langle|\mathbf{r}_N - \mathbf{r}_1|^2\rangle}{k_{\mathrm{B}}T} \qquad \textbf{[S6]}$$

is the longest relaxation time of the Rouse chain without internal friction.

For a quantitative comparison between the RIF model and experimental data, however, it is necessary to include two additional effects that are not taken into account in the original RIF model: one is the experimentally observed chain compaction at low denaturant concentrations due to the change in solvent quality, and the other is the change in the dynamics induced by the FRET dyes and the connecting linkers. To mimic chain compaction, we introduced an additional central potential

$$V_c = \sum_n k_c r_n^2/2,$$

which effectively compresses the chain towards the coordinate origin. In support of this simple approach, a comparison of the Rouse model modified in this way with more realistic simulations of a bead-and-spring model that included collapse-inducing attractive interactions showed that the behavior of both the statistical and the dynamical properties of the two models is quantitatively the same, given the same degree of chain compaction. Here, chain compaction is quantified by the ratio of its root mean square end-to-distance to that of the same chain in the absence of any attractive interactions (Fig. S4).

The donor and the acceptor dyes were represented as beads linked to the rest of the chain via harmonic springs of stiffness k_l. When the donor (D) and the acceptor (A) beads are connected, respectively, to chain beads i and j, this interaction is represented by a potential of the form

$$V_l = (1/2)k_l(\mathbf{r}_D - \mathbf{r}_i)^2 + (1/2)k_l(\mathbf{r}_A - \mathbf{r}_j)^2$$

Without this modification, the present model reproduces all of the results of Ref. (15) in the limit of zero friction. It should be noted, however, that, in contrast to Ref. (15), which predicts the existence of a maximum in the segment length dependence of the reconfiguration time, such a maximum is neither predicted by the present model nor observed experimentally.

In the absence of internal friction, the dynamics of the system is described by a straightforward generalization of the Rouse model:

$$-\boldsymbol{\xi}\frac{d\mathbf{r}}{\mathrm{dt}} - \mathbf{K}\mathbf{r} + \mathbf{f}(t) = 0$$

In addition to the coordinates of the chain beads, the vector $\mathbf{r}$ in this equation includes the coordinates of the donor bead and of the acceptor bead. $\mathbf{K}$ is the matrix of the second derivatives (Hessian) for the potential $V_0 + V_c + V_l$, $\boldsymbol{\xi}$ is a diagonal friction matrix, whose diagonal entries are the friction coefficients equal to ξ_s for each chain bead, ξ_A for the acceptor, and ξ_D for the donor. Finally, $\mathbf{f}$ is an appropriate random force vector. It is convenient to introduce a friction-scaled Hessian matrix $\tilde{\mathbf{K}}$, whose elements are given by $\tilde{K}_{ij} = K_{ij}/\sqrt{\xi_{ii}\xi_{jj}}$, and rescaled coordinates and forces, $\tilde{r}_i = r_i\sqrt{\xi_{ii}}$, $\tilde{f}_i = f_i/\sqrt{\xi_{ii}}$, in terms of which the equations of motion become

$$-\frac{d\tilde{\mathbf{r}}}{\mathrm{dt}} - \tilde{\mathbf{K}}\,\tilde{\mathbf{r}} + \tilde{\mathbf{f}}(t) = 0 \qquad \textbf{[S7]}$$

As in the Rouse model, Eq. **S7** is solved by decomposing the dynamics into those of independent relaxation modes, each of which effectively obeys overdamped harmonic oscillator dynamics. Those modes $\tilde{\mathbf{u}}_n$ are the eigenvectors of the matrix $\tilde{\mathbf{K}}$ satisfying the relation:

$$\tilde{\mathbf{K}}\tilde{\mathbf{u}}^{(n)} = (1/\tau^{(n)})\tilde{\mathbf{u}}^{(n)} \qquad \textbf{[S8]}$$

where $\tau^{(n)}$ are the corresponding relaxation times. To estimate the effective reconfiguration time for the relative motion of the donor and the acceptor, consider the autocorrelation time of their relative distance, written as a linear combination of the relaxation modes:

$$\mathbf{r}_{DA} = \mathbf{r}_D - \mathbf{r}_A = \frac{\tilde{\mathbf{r}}_D}{\sqrt{\xi_D}} - \frac{\tilde{\mathbf{r}}_A}{\sqrt{\xi_A}} = \frac{\sum_n x^{(n)}\tilde{u}_D^{(n)}}{\sqrt{\xi_D}} - \frac{\sum_n x^{(n)}\tilde{u}_A^{(n)}}{\sqrt{\xi_A}}, \qquad \textbf{[S9]}$$

where $\tilde{u}_{D,A}^{(n)}$ is the component of the nth relaxation vector that corresponds to the donor(acceptor) coordinates. The corresponding reconfiguration time τ_{DA} is estimated from the autocorrelation function

$$\tau_{DA} = \frac{\int_0^\infty dt\langle\mathbf{r}_{DA}(0)\mathbf{r}_{DA}(t)\rangle}{\langle\mathbf{r}_{DA}^2(0)\rangle} \qquad \textbf{[S10]}$$

Note that, although the timescale defined by Eq. **S10** is not identical to the experimentally estimated reconfiguration timescale, comparison with simulations of FRET in more realistic polypeptide models shows that it adequately captures the dependence of reconfiguration times on the donor and acceptor positions (15).

Eq. **S10** can be evaluated using the equipartition theorem applied to the relaxation modes. Taking advantage of their statistical independence results in the following expression for the autocorrelation functions:

$$\langle x^{(n)}(0)x^{(m)}(t)\rangle = k_{\mathrm{B}}T\tau^{(n)}e^{-t/\tau^{(n)}}\delta_{nm}, \qquad \textbf{[S11]}$$

where δ_{nm} is the Kronecker delta.

We have further assumed that, as in the original RIF model, internal friction increases each relaxation time by the same amount without affecting the structure of the eigenmodes:

$$\tau^{(n)} \to \tau^{(n)} + \tau_i \qquad \textbf{[S12]}$$

As a result, the time dependence of the correlation functions in Eq. **S11** becomes modified, but their equilibrium statistical properties are unchanged:

$$\langle x^{(n)}(0)x^{(m)}(t)\rangle = k_{\mathrm{B}}T\tau^{(n)}e^{-\frac{t}{\tau^{(n)}+\tau_i}}\delta_{nm} \qquad \textbf{[S13]}$$

Combining Eqs. **S9**, [**S10**], and [**S13**], we finally obtain:

$$\tau_{DA} = \frac{\sum_n\left(\frac{\tilde{u}_A^{(n)}}{\sqrt{\xi_A}} - \frac{\tilde{u}_D^{(n)}}{\sqrt{\xi_D}}\right)^2(\tau^{(n)})^2}{\sum_n\left(\frac{\tilde{u}_A^{(n)}}{\sqrt{\xi_A}} - \frac{\tilde{u}_D^{(n)}}{\sqrt{\xi_D}}\right)^2\tau^{(n)}} + \tau_i \qquad \textbf{[S14]}$$

To fit experimental data, the model requires the following parameters: k_c, k_l, ξ_A, ξ_D, and τ_i.

The friction of the dye ξ_D can be estimated considering that a Kuhn segment in 6M GdmCl corresponds to about five amino acids resulting in a molecular mass (approximately 600 Da) similar to that of dye and linker (643 Da for Alexa488 and 820 Da for Alexa 594), such that we assume $\xi_D = \xi_A \approx \xi_s$. Fits performed with $\xi_D = 2\xi_s$ yield results that are indistinguishable within experimental uncertainty, indicating that variation of the parameter within reasonable bounds does not affect the conclusions. The dye spring constant k_l was estimated by optimizing the fit of the model to the equilibrium interdye distances obtained from FRET efficiency histograms for the variants labeled at different positions in 7 M GdmCl, where no internal friction is present and the proteins are maximally expanded. The resulting value of k_l was then used for all other fits. Note that without including the dyes and linkers explicitly, the theory predicts a rollover in the reconfiguration time as a function of segment length when $|i\text{-}j|$ approaches the total number of segments (15), which is not observed experimentally. The confining spring constant k_c was adjusted such that the change in dimensions obtained from FRET efficiency histograms at different GdmCl concentrations relative to the maximally expanded state in 7 M GdmCl was reproduced. In this way the only remaining free parameter is the internal friction time τ_i, which is obtained from fitting the model to the position dependence of the reconfiguration times (Fig. 3). The τ_i extracted with this procedure is given relative to the τ_s obtained by the model at the same GdmCl concentration. In order to compare this result with values of internal friction obtained from the viscosity dependence, the ratio $\left(\frac{\tau_i}{\tau_{ij,(i=1,j=67)}}\right)_{\text{positiondependence}}$ was multiplied by the corresponding measured reconfiguration time of the end-to-end variant, τ_r, obtained at the same GdmCl concentration. Note that the uncertainty of τ_i determined in this way increases for large values of τ_i (Fig. 4) because the deviation of τ_{ij}/τ_r from a value of 1 becomes comparable to the experimental error.

Comparison of the effects of specific and nonspecific collapse on the chain dynamics. It could be argued that simple polymer models applied to unfolded proteins, especially under near-native conditions, are too unrealistic as they fail to capture the formation of partial secondary structure or specific hydrophobic clusters within the chain. Here we use simulations to argue (1) that experimental data can be used to differentiate nonspecific collapse assumed by such models from structural ordering and (2) that our experimental results, even at the lowest denaturant concentrations, where the conditions are close to native, are more consistent with the nonspecific collapse scenario. Specifically, we have simulated a variant of the generalized Rouse model (GRM) of Thirumalai and coworkers (16, 17) to mimic the formation of specific structural order within a chain by introducing an attractive interaction between an individual pair of monomers. An example of such a computation (Fig. S7) shows that the chain segment length dependence of both the intramonomer distance $r_{ij} = \langle|\mathbf{r}_j - \mathbf{r}_i|^2\rangle^{1/2}$ and reconfiguration time τ_{ij} found for a chain with attractive interactions between an individual pair of monomers is qualitatively different from both our experimental findings and from simple polymer models that assume nonspecific collapse. This finding suggests that specific structural ordering at low denaturant concentrations cannot explain our experimental results.

1. Nettels D, Gopich IV, Hoffmann A, Schuler B (2007) Ultrafast dynamics of protein collapse from single-molecule photon statistics. *Proc Natl Acad Sci USA* 104:2655–2660.
2. Nettels D, Hoffmann A, Schuler B (2008) Unfolded protein and peptide dynamics investigated with single-molecule FRET and correlation spectroscopy from picoseconds to seconds. *J Phys Chem B* 112:6137–6146.
3. Doose S, Neuweiler H, Sauer M (2005) A close look at fluorescence quenching of organic dyes by tryptophan. *Chemphyschem* 6:2277–2285.
4. Hoffmann A, et al. (2007) Mapping protein collapse with single-molecule fluorescence and kinetic synchrotron radiation circular dichroism spectroscopy. *Proc Natl Acad Sci USA* 104:105–110.
5. Müller-Späth S, et al. (2010) Charge interactions can dominate the dimensions of intrinsically disordered proteins. *Proc Natl Acad Sci USA* 107:14609–14614.
6. Hofmann H, et al. (2010) Single-molecule spectroscopy of protein folding in a chaperonin cage. *Proc Natl Acad Sci USA* 107:11793–11798.
7. Pfeil SH, Wickersham CE, Hoffmann A, Lipman EA (2009) A microfluidic mixing system for single-molecule measurements. *Rev Sci Instrum* 80:055105.
8. Gösch M, Blom H, Holm J, Rigler R (2000) Hydrodynamic flow profiling in microchannel structures by single molecule fluorescence spectroscopy. *Anal Chem* 72:3260–3265.
9. Schuler B (2007) Application of single molecule Förster resonance energy transfer to protein folding. *Methods Mol Biol* 350:115–138.
10. Kawahara K, Tanford C (1966) Viscosity and density of aqueous solutions of urea and guanidine hydrochloride. *J Biol Chem* 241:3228–3232.
11. Schuler B, Lipman EA, Steinbach PJ, Kumke M, Eaton WA (2005) Polyproline and the "spectroscopic ruler" revisited with single molecule fluorescence. *Proc Natl Acad Sci USA* 102:2754–2759.
12. Thirumalai D, Ha BY (1988) *Theoretical and Mathematical Models in Polymer Research*, ed Grosberg A (Academia, New York), pp 1–35.
13. Doi M, Edwards SF (1988) *The Theory of Polymer Dynamics* (Oxford University Press, USA, New York).
14. Nettels D, et al. (2009) Single molecule spectroscopy of the temperature-induced collapse of unfolded proteins. *Proc Natl Acad Sci. USA* 106:20740–20745.
15. Makarov DE (2010) Spatiotemporal correlations in denatured proteins: The dependence of fluorescence resonance energy transfer (FRET)-derived protein reconfiguration times on the location of the FRET probes. *J Chem Phys* 132:035104.
16. Barsegov V, Morrison G, Thirumalai D (2008) Role of internal chain dynamics on the rupture kinetic of adhesive contacts. *Phys Rev Lett* 100:248102.
17. Hyeon C, Morrison G, Thirumalai D (2008) Force-dependent hopping rates of RNA hairpins can be estimated from accurate measurement of the folding landscapes. *Proc Natl Acad Sci USA* 105:9604–9609.

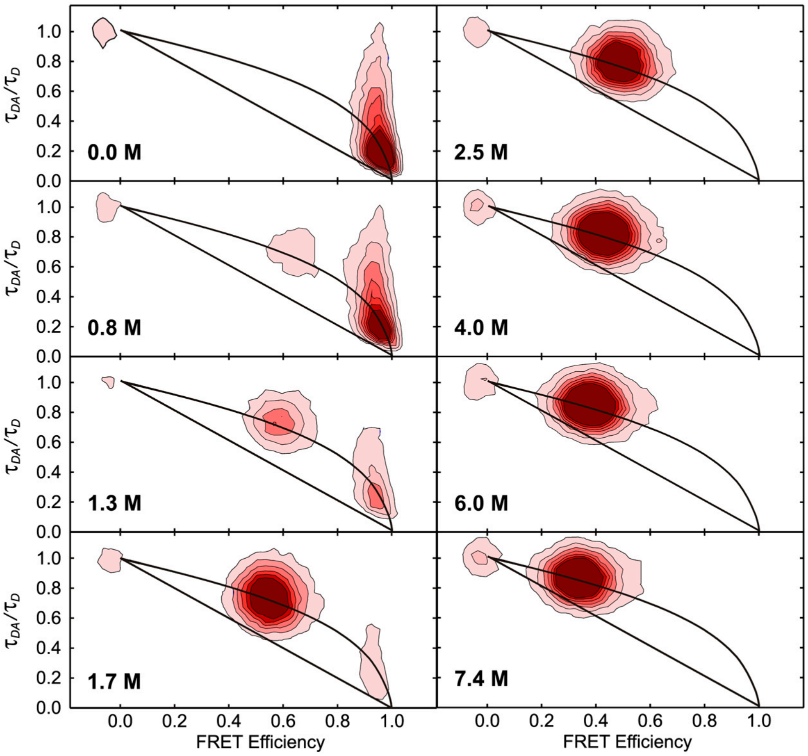

Fig. S1. Two-dimensional histograms of relative donor lifetime versus FRET efficiency measured between 0 M and 7.4 M GdmCl (cf. Fig. 1, main text). τ_{DA} and τ_D are the donor fluorescence lifetimes in presence and in absence of acceptor, respectively. For details, see *Fluorescence lifetimes and FRET efficiencies*.

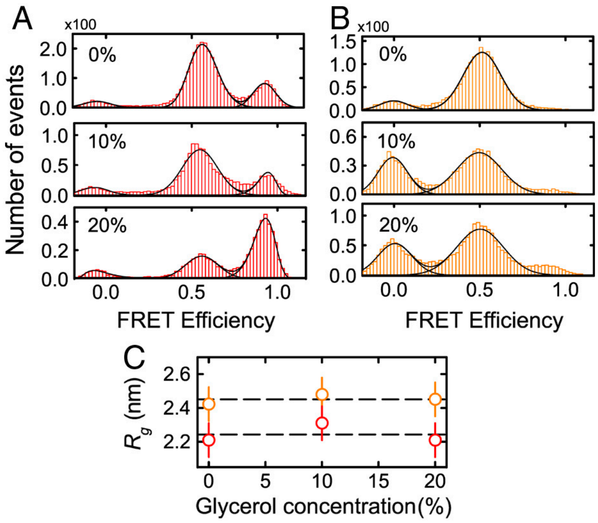

Fig. S2. FRET efficiency histograms of Csp at 1.3 M (*A*) and 2 M (*B*) GdmCl with different concentrations of glycerol (% by mass). At 1.3 M GdmCl and 20% glycerol, the denaturant concentration was adjusted slightly to 1.4 M GdmCl to counteract the effect of stabilization of the native state while maintaining the same transfer efficiency. Generally, the presence of glycerol in solution did not affect the radius of gyration of the chain significantly, as shown in (*C*) (colors as in *A*, *B*). The same behavior was observed at 4 M and 6 M GdmCl.

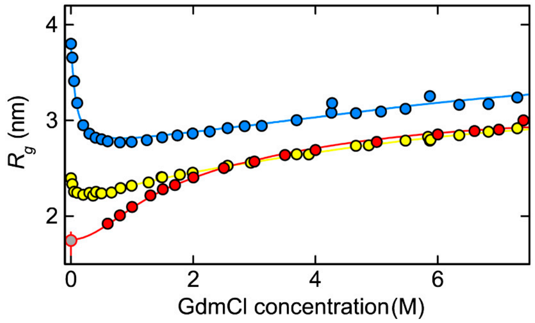

Fig. S3. Radii of gyration, R_g, for Csp (red), IN (yellow), and ProTα (blue) obtained assuming the distance distribution of a Gaussian chain. Very similar results are obtained with other distance distributions (5). The data for IN and ProTαC were fit as described previously (5). The expansion of IN and ProTα at low GdmCl concentration is due to charge repulsion at low ionic strength (5). For interpolation, the Csp data were fit with $R_g = R_{g0}(1 + \rho K_b a/(1 + K_b a))$, where R_{g0} is the dimension in the absence of denaturant, ρ is a scaling constant, K_b is an effective binding constant of denaturant to the chain, and a is the activity of the denaturant (5, 14). The residual difference in chain dimensions at high denaturant concentrations may be due to excluded volume effects from the long unlabeled polypeptide tail in ProTα or GdmCl binding to acidic side chains (5). The gray data point is from the microfluidic mixing experiment (see Fig. 4, main text).

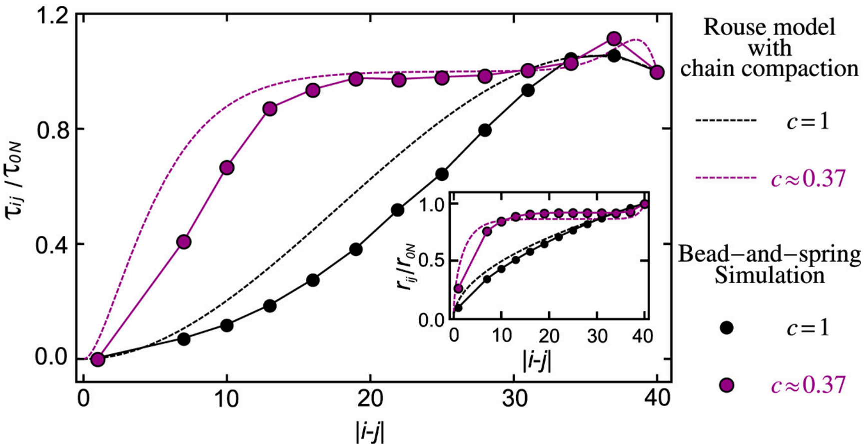

Fig. S4. Justification for using a simple harmonic potential to mimic chain collapse within the extended RIF. In the extended RIF, chain compaction is induced by applying a parabolic trapping potential to every chain monomer. Here we show that such a model realistically reproduces the properties of a chain undergoing a coil-to-globule transition. To simulate the coil-globule transition, we used a chain of $N = 41$ beads connected by harmonic springs. In addition, nonbonded beads interacted via a Lennard-Jones potential. Chain collapse was induced by lowering the temperature and quantified by the compactness parameter c equal to the ratio of the chain's root mean square distance to the root mean square distance corresponding to the high temperature limit (such that $c = 1$ at high temperature, in the absence of collapse). The reconfiguration time, τ_{ij}, and the rms distance, r_{ij}, plotted as a function of the length of the chain segment between the monomers i and j, agree well with those computed for a Rouse chain, in which collapse was introduced by applying a potential $k_c r^2/2$ to each monomer. Again, the degree of collapse for the Rouse chain was quantified by the compactness parameter c, taken, in this case, to be the ratio of the rms end-to-end distance to that for $k_c = 0$. Given the same values of the compactness parameter, the results for the Rouse model agree quite well with those for the bead-and-spring model, especially considering that the Rouse model does not take into account excluded volume effects. Here we only show the data for extreme cases of no compaction and very strong compaction (where c is smaller than the typical experimental values); similar agreement was observed for intermediate values of c (data not shown).

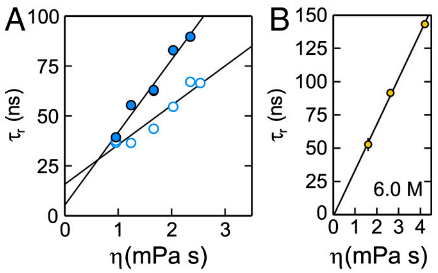

Fig. S5. (*A*) Viscosity dependence of the reconfiguration time of ProTα in native buffer (filled circles) and upon addition of 1 M KCl (empty circles). Data were fit globally as for the Csp viscosity dependence (Fig. 2), which resulted in values of the internal friction time of (6 ± 5) ns and (16 ± 3) ns without and with salt, respectively. (*B*) Viscosity dependence of the reconfiguration time of IN in 6 M GdmCl. The linear fit yields a value for the internal friction time of (-2 ± 6) ns, indicating that internal friction is negligible at high GdmCl concentrations.

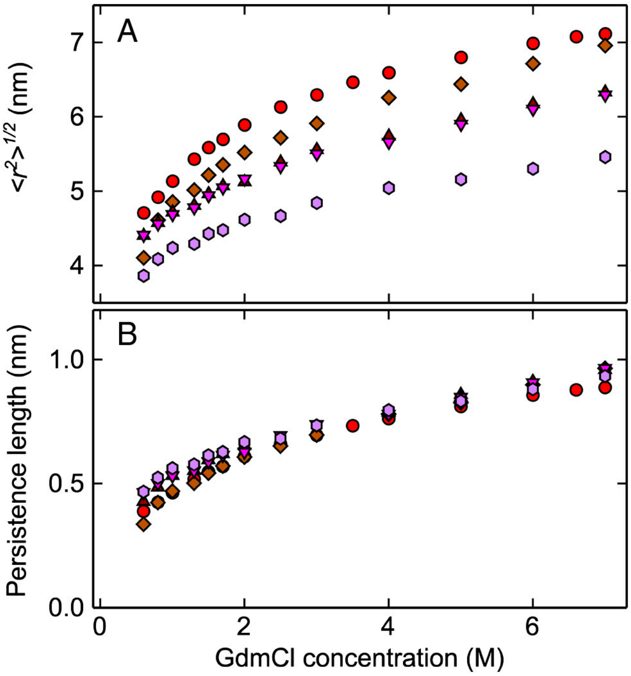

Fig. S6. Root mean squared interdye distances and persistence lengths as a function of GdmCl concentration for the different Csp variants (CspC2C68, red circles; CspC10C67 brown diamonds; CspC21C67, dark red triangles up; CspC22C67, pink triangles down; CspC36C69 violet hexagons). The good agreement of the persistence lengths indicates a uniform collapse of the chain (4) and thus the dominance of nonspecific interactions in driving collapse and causing internal friction.

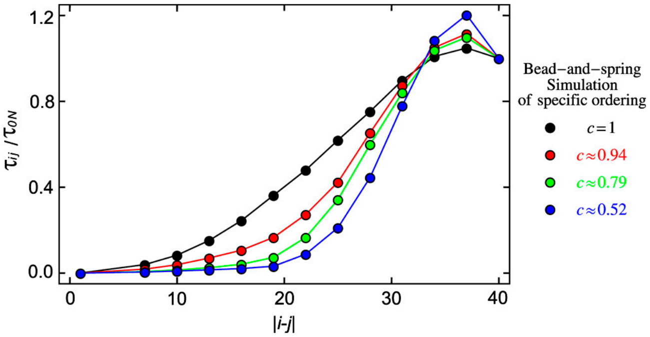

Fig. S7. Specific intrachain interactions result in spatio-temporal correlations within the polymer chain that are quite different from those observed experimentally and in simulations of nonspecific collapse. Here, we illustrate this using a generalized Rouse-type model (16, 17), in which a pair of monomers within a bead-and-spring chain model interact via an attractive potential. We use a chain with $N = 41$ beads, where the 4th and the 36th beads attract one another. We have also considered other choices of the two monomers (data not shown), leading to similar conclusions. As the strength of the attractive potential increases, more compact configurations are favored. Again, we characterize this compaction in terms of the compactness parameter c, equal to the ratio of the end-to-end distance and the end-to-end distance in the limit of no attractive interaction. The effect of chain compaction on the reconfiguration times τ_{ij} is very different from that observed in the experiments and in our simulations of chains without specific interactions (cf. Fig. S4). Specifically, more compact chains exhibit a τ_{ij} that decreases more precipitously with decreasing length of the chain segment $|i\text{-}j|$ between the monomers, in contrast to the weakening of this dependence observed experimentally at lower denaturant concentrations (Fig. 3) as well as predicted by the models that do not include monomer-specific interactions.

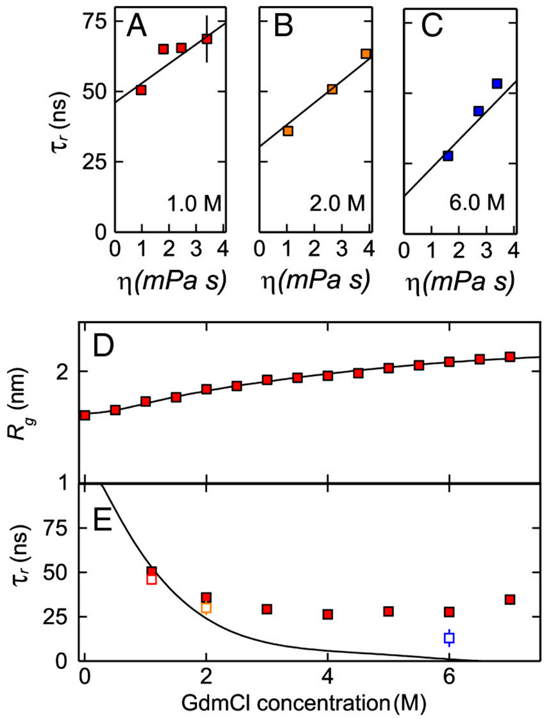

Fig. S8. Reconfiguration dynamics and internal friction of the bisected variant of CspC36C69 (see Tab. S1). Viscosity dependences of reconfiguration times, τ_r, at 1.0 M (*A*), 2.0 M (*B*), and 6.0 M GdmCl (*C*), respectively. The data were fit globally as in Fig. 2 (solid lines). (*D*) Denaturant dependence of the radius of gyration, R_g. (*E*) Reconfiguration times τ_r of the bisected variant (red filled squares) compared with the values of internal friction times obtained from the viscosity dependences (*A*–*C*) (empty squares, colors as in *A*–*C*), and with internal friction times of full length CspC2C68 (black line, from Fig. 4*A*). The good agreement of friction times in the two variants indicates the importance of local interactions for internal friction.

Table S1. Amino acid sequences of the variants of Csp from *Thermotoga maritima* used in this work (mutations relative to wt in bold, fluorophore labeling positions in bold underline)

		1 10 20 30 40 50 60
Csp(wild type)		MRGKVKWFDS KKGYGFITKD EGGDVFVHWS AIEMEGFKTL KEGQVVEFEI QEGKKGPQAA HVKVVE
CspC67	MAHHHHHHSWAALEVLFQ GPG	MRGKVK**F**FDS KKGYGFITKD EGGDVFVH**F**S AIEMEGFKTL KEGQVVEFEI QEGKKG**G**QAA HVKVVE**C**
CspC2C68	MAHHHHHHSWAALEVLFQ GPG	M**C**RGKVK**F**FD SKKGYGFITK DEGGDVFVH**F** SAIEMEGFKT LKEGQVVEFE IQEGKKG**G**QA AHVKVVE**C**
CspC10C67	MAHHHHHHSWAALEVLFQ GPG	MRGKVK**F**FD**C** KKGYGFITKD EGGDVFVH**F**S AIEMEGFKTL KEGQVVEFEI QEGKKG**G**QAA HVKVVE**C**
CspC21C67	MAHHHHHHSWAALEVLFQ GPG	MRGKVK**F**FDS KKGYGFITKD **C**GGDVFVH**F**S AIEMEGFKTL KEGQVVEFEI QEGKKG**G**QAA HVKVVE**C**
CspC22C67	MAHHHHHHSWAALEVLFQ GPG	MRGKVK**F**FDS KKGYGFITKD E**C**GDVFVH**F**S AIEMEGFKTL KEGQVVEFEI QEGKKG**G**QAA HVKVVE**C**
CspC36C69	MAHHHHHHSWAALEVLFQ GPG	MRGKVK**F**FDS KKGYGFITKD EGGDVFVH**F**S AIEGR**C**EGFK TLKEGQVVEF EIQEGKKG**G**Q AAHVKVVE**C**
CspC36C69 bisected		**C**EGFK TLKEGQVVEF EIQEGKKG**G**Q AAHVKVVE**C**

Proline was removed to eliminate a kinetic component due to cis/trans isomerization (2, 3, 16); Trp residues were replaced by Phe to eliminate static quenching of the internally labeled variants. The hexahistidine tag (blue) was removed by digest with HRV 3C protease. For CspC36C69 a Factor Xa protease site was introduced (underline) to allow preparation of a bisected variant lacking the N-terminal tail

Supporting Information

Soranno et al. 10.1073/pnas.1117368109

SI Text

SI Materials and methods. ***Protein preparation and labeling.*** Five different variants of Csp were prepared starting from a DNA sequence with an additional C-terminal cysteine (Table S1, CspC67). In contrast to the terminal positions, which are not influenced by quenching (1), previously published results on reconfiguration dynamics in the internal positions of Csp (2) were found to be affected by quenching of the FRET dyes by Trp side chains. Here we avoid this complication by replacing all Trp residues in the protein by Phe, which does not quench donor or acceptor (3). This lack of quenching is reflected by a more pronounced anticorrelation in the donor-acceptor cross-correlation functions (Fig. 1). The good agreement of the reconfiguration times obtained for the terminally labeled variant used here and the terminally labeled protein containing both Trp residues (1) (note that no fluorophore quenching is observed for the terminally labeled variant in both cases), indicates that the Trp to Phe exchanges do not affect unfolded state dynamics significantly. Several second cysteine residues were introduced by site-directed mutagenesis to provide specific labeling positions for the dyes (see Table S1 for all amino acid sequences). All variants were expressed with an N-terminal hexahistidine tag containing a tryptophan residue to facilitate detection and quantification by UV-Vis spectroscopy during purification. After purification, the proteins were digested with HRV 3C protease to cleave off the His-tag. The sequence CspC36C69 contains an additional protease cleavage site (Factor Xa) N-terminal to Cys36 for the preparation of a bisected variant that enables a comparison of the full length protein and the shortened peptide corresponding to the C-terminal segment alone. The synthetic starting gene (Celtek Bioscience) was cloned into vector pET47b (+). The variants were expressed in E. coli BL21 (DE3) and purified from the inclusion bodies using a HisTrap column (GE Healthcare, BioSciences AB) in 20 mM Tris-HCl, 0.5 M NaCl, 2 mM β-mercaptoethanol, 20 mM imidazole, 4 M GdmCl, pH 8.0 and elution with an imidazole gradient. The resulting protein was dialyzed against 50 mM sodium phosphate, 0.5 mM EDTA, 2 mM β-mercaptoethanol, pH 7.4 and digested by adding HRV 3C protease (containing a His-tag; 1mg HRV 3C per 55 mg Csp). Finally, digested Csp was separated from protease, uncleaved Csp, and free His-tag by a second HisTrap chromatography run. Labeling was performed as described previously (2, 4) and verified by mass spectrometry. IN and ProTα were expressed, purified, and labeled as described previously (5).

Single-molecule fluorescence spectroscopy. Single-molecule fluorescence measurements were performed with a MicroTime 200 confocal microscope (PicoQuant, Berlin, Germany) equipped with a diode laser (LDH-D-C-485, PicoQuant), a HeNe laser (594 nm, CWI Melles Griot) and an Olympus UplanApo 60x/1.20W objective (Olympus). Emitted photons were collected through the microscope objective, focused onto a 100 μm pinhole and then separated into four channels with a polarizing beam splitter and a dichroic mirror (585DCXR, Chroma). Photons emitted by the acceptor dye were additionally filtered (HQ650/100 Chroma Technology) and then focused onto a SPAD detector (Perkin Elmer). Photons emitted by the donor dye were filtered (ET525/50M, Chroma Technology) and detected with an avalanche photodiode (MPD, PDM series, 50 μm, PicoQuant). The arrival time of every detected photon was recorded by a HydraHarp 400 counting module (PicoQuant), and the time between excitation pulse and photon detection pulse was stored with 4 ps resolution (time resolution was thus limited by the timing jitter of the detectors).

The donor dye was excited with an average power of 100 μW. Single-molecule FRET efficiency histograms were acquired in samples with protein concentrations of about 20 pM to 50 pM; detected photons were recorded with a time resolution of 16 ps, with the laser in pulsed mode at a repetition rate of 64 MHz. Nanosecond-FCS measurements were performed in samples with a protein concentration of approximately 1 nM, with the laser in continuous wave mode, with typical data acquisition times of 10 to 16 h. Control measurements to determine the contribution of quenching to the acceptor intensity autocorrelation were carried out by exciting with a continuous wave HeNe laser (594 nm, CVI Melles Griot) at a power of 16 μW. All measurements were performed in 50 mM sodium phosphate buffer, pH 7.0, 150 mM β-mercaptoethanol, and 0.001% Tween 20 (Pierce) with varying concentrations of GdmCl. 20 mM cysteamine were added to enhance the fluorophore brightness and minimize bleaching.

Rapid mixing experiments were performed essentially as described by Hofmann et al. (6). Microfluidic mixers fabricated by replica molding in polydimethylsiloxane (PDMS) were used (6, 7). 200 pM of terminally labeled Csp unfolded in 1.5 M GdmCl from the inlet channel (from the left in Fig. 4*B*) were mixed with buffer without denaturant from the side channels (from the top and bottom in Fig. 4*B*), resulting in a final concentration of 0.25 M GdmCl in the observation channel (to the right in Fig. 4*B*). 0.015 % Tween 20 were included to prevent nonspecific interactions of the protein with the PDMS surfaces. Measurements were taken by placing the confocal volume at a position 50 μm (8 ms) downstream of the mixing region. The experiments were performed with pressures of 13.8 kPa (2.0 psi) applied to all channels. To estimate the time after mixing, the calculated average fully developed flow velocity of 1.2 mm/s (13.8 kPa) in the observation channel was corrected by accounting for the change in width of the observation channel from the mixing area to the observation point, as described by Pfeil et al. (7). The stability of the flow velocity during the measurements was confirmed by analyzing the donor-acceptor fluorescence intensity cross-correlation functions (8). nsFCS measurements were taken for 6 h and analyzed as described below (in *Nanosecond-FCS measurements*).

The viscosities of the solutions were measured with a digital viscometer (DV-I+, Brookfield Engineering) with a CP40 spindle and 30–60 rpm, which allows determination of viscosity with an uncertainty of 0.05 to 0.1 mPa s. The calibration of the instrument was tested with a reference solution of known viscosity. The changes in refractive index caused by the addition of viscogens and/or denaturant were determined with a digital Abbe refractometer (Krüss, Germany) and were taken into account for the calculation of the Förster radii for the corresponding solution conditions.

Data analysis. ***Fluorescence lifetimes and FRET efficiencies.*** The average fluorescence lifetimes were estimated as the mean detection time of the burst photons after donor excitation. The transfer efficiencies were obtained from $E = n_A/(n_A + n_D)$, where n_D and n_A are the numbers of donor and acceptor photons in the burst corrected for background, channel crosstalk, acceptor direct excitation, differences in quantum yields of the dyes, and detection efficiencies (9). For a fixed distance r, the mean donor lifetime in the presence of acceptor is given by $\tau_{DA} = \tau_{DA}(r) = \tau_D(1 - E(r))$, where τ_D is the lifetime in the absence of acceptor and $E(r) = 1/(1 + R_0^6/r^6)$, with the Förster radius R_0 calculated for the respective values of the refractive index of the solution (10) (black straight line in Fig. 1*B*). For a chain with a probability density function $P(r)$ of the interdye distance r, $\tau_{DA} = \int_0^\infty tI(t)\mathrm{d}t / \int_0^\infty I(t)\mathrm{d}t$ with $I(t) = I_0 \int_0^\infty P(r) e^{-t/\tau_{DA}(r)}\mathrm{d}r$, where I is the time-dependent fluorescence emission intensity, and the mean FRET efficiency is calculated as $\langle E \rangle = \int_0^\infty E(r)P(r)\mathrm{d}r$. In Fig. 1*b*, a Gaussian chain distribution for the distances

$$P_{\mathrm{Gauss}}(r) = 4\pi r^2 \left(\frac{3}{2\pi \langle r^2 \rangle} \right)^{3/2} e^{-\frac{3r^2}{2\langle r^2 \rangle}}, \qquad \textbf{[S1]}$$

(where $\langle r^2 \rangle$ is the mean squared end-to-end distance of the segment probed) and the distribution of distances for a worm-like chain (11, 12) were compared. The resulting parametric plots are shown as the curved solid line (Gaussian chain) and the curved dashed line (worm-like chain), respectively. For the Gaussian chain, the corresponding radius of gyration, R_g, can be calculated from $R_g^2 = \langle r^2 \rangle / 6$. This conversion is used for the inset of Fig. 5 (main text) and for Figs. S2 and S6. For calculating persistence lengths, l_p, (Fig. S5), we use $l_p = \langle r^2 \rangle / 2l_c$, where l_c is the contour length of the segment probed (13), with corrections for dyes and linkers, as described previously (4). The insensitivity of the result to the detailed model used for the distance distribution is largely due to the similarity of the shape of the different distributions around their mean values given the low persistence lengths relative to the contour lengths of the polypeptides investigated here (5). Note that the long-range reconfiguration times observed here are much greater than the fluorescence lifetimes of the dyes; the effect of chain dynamics on the observed transfer efficiencies is thus negligible (14).

Nanosecond-FCS measurements. Autocorrelation curves of acceptor and donor channels and cross-correlation curves between acceptor and donor channels were calculated from measurements as described previously (1, 2). The data were fit over a time window of 4 μs with

$$g_{ij}(\tau) = 1 + \frac{1}{N}\left(1 - c_{\mathrm{AB}} e^{-\frac{t-t_0}{\tau_{\mathrm{AB}}}}\right)\left(1 + c_{\mathrm{CD}} e^{-\frac{t-t_0}{\tau_{\mathrm{CD}}}}\right)\left(1 + c_T e^{-\frac{t-t_0}{\tau_T}}\right), \quad i, j = A, D, \qquad \textbf{[S2]}$$

where N is the mean number of molecules in the confocal volume. The three multiplicative terms describe the contribution to amplitude and timescale of photon antibunching (AB), chain dynamics (CD), and triplet blinking of the dyes (T). In the case of the Csp variants, the three correlation curves were fit globally with the same values of τ_{CD} and t_0 above 1.5 M GdmCl. The amplitude and the lifetime of the antibunching and triplet component were fit with a free independent decay component for each correlation curve. Triplet lifetimes show a systematic increase in the range between 2 μs and 4 μs as the GdmCl concentration increases from 0 M to 7 M. Below 1.5 M GdmCl, only the donor autocorrelation was taken into account due to a significant contribution from the native state in the acceptor autocorrelation. The same approach was used for IN due to the presence of static quenching in the acceptor under native conditions. In the case of ProTα, data were fit globally over the entire range of GdmCl concentrations.

An estimation of the errors for Csp data has been obtained performing a Bootstrap-method, randomly sampling 50 subdatasets from the original dataset and fitting them with the same model. The obtained results have been used to estimate a standard deviation error from the mean. The resulting correlation times, τ_{CD}, can be described in terms of diffusion on the potential of mean force that corresponds to the $P(r)$ determined from the FRET efficiencies and fluorescence lifetimes and then converted in the reconfiguration time of the polypeptide chain (1).

Global fit of viscosity dependence of τ_r. The viscosity-dependent reconfiguration times measured at different GdmCl concentrations (Fig. 2) were fit globally according to Eq. **2** and **3** with $(\tau_r)_{\mathrm{GdmCl}} = a \cdot \langle r^2 \rangle_{\mathrm{GdmCl}} \eta/\eta_0 + (\tau_i)_{\mathrm{GdmCl}}$, where $\langle r^2 \rangle_{\mathrm{GdmCl}}$ is the mean square end-to-end distance of the chain as determined from single-molecule FRET experiments at a given GdmCl concentration, $(\tau_i)_{\mathrm{GdmCl}}$ is the "dry" internal friction contribution at the same GdmCl concentration, and a is a proportionality constant common to all GdmCl concentrations. According to the Rouse model, a can be related to the diffusion coefficient D_0 of a chain segment through $a = \frac{N}{3\pi^2 D_0}$ (13). Assuming that N equals the number of Kuhn segments (including the contribution of dyes and linkers), we obtain a value of $D_0 = (0.73 \pm 0.03) \cdot 10^{-5}\ \mathrm{cm}^2/\mathrm{s}$, in a reasonable range for our segment size. The global fit describes the observed behavior at all the denaturant conditions well, as shown in Fig. 2, suggesting that if there is a contribution from "wet" friction, it would be the same irrespective of the solvent.

The viscosity dependences of the bisected variant of Csp at different GdmCl concentrations were fit globally as the data of the full length protein (Fig. S8). The global fit provides an estimate of the internal friction times, with 45 ± 4 ns, 29 ± 5 ns, and 12 ± 6 ns at 1.0 M, 2.0 M, and 6.0 M GdmCl, respectively. The proportionality constant a in the global fit was converted to diffusion coefficient of the elementary segment D_0 as explained for the full length variant. In this case, $D_0 = (0.7 \pm 0.2) \cdot 10^{-5}\ \mathrm{cm}^2/\mathrm{s}$, in excellent agreement with the value for the full length protein, suggesting that the model does not only provide the correct scaling with the mean squared end-to-end distance, but also the correct scaling with the length of the sequence.

Extended RIF model. The Rouse model with internal friction (RIF) assumes that a polymer chain obeys the following equations of motion:

$$-\xi_s \frac{d\mathbf{r}}{\mathrm{d}t} - \xi_i \mathbf{k} \frac{d\mathbf{r}}{\mathrm{d}t} - k_0 \mathbf{k}\mathbf{r} + \mathbf{f}(t) = 0 \qquad \textbf{[S3]}$$

Here $\mathbf{r}$ is the vector whose components are the positions of the polymer beads, k_0 is the stiffness of the spring connecting two adjacent beads, ξ_s and ξ_i are, respectively, the solvent- and the internal friction coefficients, $\mathbf{f}(t)$ is a random force vector satisfying the appropriate fluctuation-dissipation relationship, and $\mathbf{k}$ is a dimensionless connectivity matrix such that $k_0\mathbf{k}$ is the stiffness (Hessian) matrix of the chain. Specifically, this matrix is tridiagonal:

$$\mathbf{k} = \begin{bmatrix} -1 & 1 & 0 & 0 & \dots \\ 1 & -2 & 1 & 0 & \dots \\ 0 & 1 & -2 & 1 & \dots \\ 0 & 0 & 1 & -2 & \dots \\ \dots & \dots & \dots & \dots & \dots \end{bmatrix}$$

These equations describe the Brownian dynamics of a linear chain of N beads with coordinates $\mathbf{r}_1, \mathbf{r}_2, \ \dots.. \ , \mathbf{r}_N$, connected by harmonic springs such that the total potential energy is given by

$$V_0 = \frac{k_0}{2} \sum_{n=2}^{N} (\mathbf{r}_n - \mathbf{r}_{n-1})^2 \qquad \textbf{[S4]}$$

The mathematical structure of RIF is such that both the chain's stiffness matrix and the "friction matrix" $\xi_i\mathbf{k}$ appearing in the second term of Eq. **S3** are proportional to the same connectivity matrix. This results in a particularly simple eigenmode spectrum, where the presence of internal friction does not change the eigenmodes of the system (which remain identical to the Rouse modes), but shifts all of its characteristic times by a constant amount,

$$\tau^{(n)} = (\tau_{\text{Rouse}}/n^2) + \tau_i, \qquad n = 1, 2, \ldots \qquad \textbf{[S5]}$$

where $\tau_i = \xi_i/k_0$ is the timescale associated with internal friction, and

$$\tau_{\text{Rouse}} = \frac{\xi_s}{3\pi^2} \frac{N\langle|\mathbf{r}_N - \mathbf{r}_1|^2\rangle}{k_{\text{B}}T} \qquad \textbf{[S6]}$$

is the longest relaxation time of the Rouse chain without internal friction.

For a quantitative comparison between the RIF model and experimental data, however, it is necessary to include two additional effects that are not taken into account in the original RIF model: one is the experimentally observed chain compaction at low denaturant concentrations due to the change in solvent quality, and the other is the change in the dynamics induced by the FRET dyes and the connecting linkers. To mimic chain compaction, we introduced an additional central potential

$$V_c = \sum_n k_c r_n^2/2,$$

which effectively compresses the chain towards the coordinate origin. In support of this simple approach, a comparison of the Rouse model modified in this way with more realistic simulations of a bead-and-spring model that included collapse-inducing attractive interactions showed that the behavior of both the statistical and the dynamical properties of the two models is quantitatively the same, given the same degree of chain compaction. Here, chain compaction is quantified by the ratio of its root mean square end-to-distance to that of the same chain in the absence of any attractive interactions (Fig. S4).

The donor and the acceptor dyes were represented as beads linked to the rest of the chain via harmonic springs of stiffness k_l. When the donor (D) and the acceptor (A) beads are connected, respectively, to chain beads i and j, this interaction is represented by a potential of the form

$$V_l = (1/2)k_l(\mathbf{r}_D - \mathbf{r}_i)^2 + (1/2)k_l(\mathbf{r}_A - \mathbf{r}_j)^2$$

Without this modification, the present model reproduces all of the results of Ref. (15) in the limit of zero friction. It should be noted, however, that, in contrast to Ref. (15), which predicts the existence of a maximum in the segment length dependence of the reconfiguration time, such a maximum is neither predicted by the present model nor observed experimentally.

In the absence of internal friction, the dynamics of the system is described by a straightforward generalization of the Rouse model:

$$-\boldsymbol{\xi}\frac{d\mathbf{r}}{\text{dt}} - \mathbf{K}\mathbf{r} + \mathbf{f}(t) = 0$$

In addition to the coordinates of the chain beads, the vector $\mathbf{r}$ in this equation includes the coordinates of the donor bead and of the acceptor bead. $\mathbf{K}$ is the matrix of the second derivatives (Hessian) for the potential $V_0 + V_c + V_l$, $\boldsymbol{\xi}$ is a diagonal friction matrix, whose diagonal entries are the friction coefficients equal to ξ_s for each chain bead, ξ_A for the acceptor, and ξ_D for the donor. Finally, $\mathbf{f}$ is an appropriate random force vector. It is convenient to introduce a friction-scaled Hessian matrix $\tilde{\mathbf{K}}$, whose elements are given by $\tilde{K}_{ij} = K_{ij}/\sqrt{\xi_{ii}\xi_{jj}}$, and rescaled coordinates and forces, $\tilde{r}_i = r_i\sqrt{\xi_{ii}}$, $\tilde{f}_i = f_i/\sqrt{\xi_{ii}}$, in terms of which the equations of motion become

$$-\frac{d\tilde{\mathbf{r}}}{\text{dt}} - \tilde{\mathbf{K}}\,\tilde{\mathbf{r}} + \tilde{\mathbf{f}}(t) = 0 \qquad \textbf{[S7]}$$

As in the Rouse model, Eq. **S7** is solved by decomposing the dynamics into those of independent relaxation modes, each of which effectively obeys overdamped harmonic oscillator dynamics. Those modes $\tilde{\mathbf{u}}_n$ are the eigenvectors of the matrix $\tilde{\mathbf{K}}$ satisfying the relation:

$$\tilde{\mathbf{K}}\tilde{\mathbf{u}}^{(n)} = (1/\tau^{(n)})\tilde{\mathbf{u}}^{(n)} \qquad \textbf{[S8]}$$

where $\tau^{(n)}$ are the corresponding relaxation times. To estimate the effective reconfiguration time for the relative motion of the donor and the acceptor, consider the autocorrelation time of their relative distance, written as a linear combination of the relaxation modes:

$$\mathbf{r}_{DA} = \mathbf{r}_D - \mathbf{r}_A = \frac{\tilde{\mathbf{r}}_D}{\sqrt{\xi_D}} - \frac{\tilde{\mathbf{r}}_A}{\sqrt{\xi_A}} = \frac{\sum_n x^{(n)}\tilde{u}_D^{(n)}}{\sqrt{\xi_D}} - \frac{\sum_n x^{(n)}\tilde{u}_A^{(n)}}{\sqrt{\xi_A}}, \qquad \textbf{[S9]}$$

where $\tilde{u}_{D,A}^{(n)}$ is the component of the nth relaxation vector that corresponds to the donor(acceptor) coordinates. The corresponding reconfiguration time τ_{DA} is estimated from the autocorrelation function

$$\tau_{DA} = \frac{\int_0^\infty dt\langle\mathbf{r}_{DA}(0)\mathbf{r}_{DA}(t)\rangle}{\langle\mathbf{r}_{DA}^2(0)\rangle} \qquad \textbf{[S10]}$$

Note that, although the timescale defined by Eq. **S10** is not identical to the experimentally estimated reconfiguration timescale, comparison with simulations of FRET in more realistic polypeptide models shows that it adequately captures the dependence of reconfiguration times on the donor and acceptor positions (15).

Eq. **S10** can be evaluated using the equipartition theorem applied to the relaxation modes. Taking advantage of their statistical independence results in the following expression for the autocorrelation functions:

$$\langle x^{(n)}(0)x^{(m)}(t)\rangle = k_{\text{B}}T\tau^{(n)}e^{-t/\tau^{(n)}}\delta_{nm}, \qquad \textbf{[S11]}$$

where δ_{nm} is the Kronecker delta.

We have further assumed that, as in the original RIF model, internal friction increases each relaxation time by the same amount without affecting the structure of the eigenmodes:

$$\tau^{(n)} \to \tau^{(n)} + \tau_i \qquad \textbf{[S12]}$$

As a result, the time dependence of the correlation functions in Eq. **S11** becomes modified, but their equilibrium statistical properties are unchanged:

$$\langle x^{(n)}(0)x^{(m)}(t)\rangle = k_{\text{B}}T\tau^{(n)}e^{-\frac{t}{\tau^{(n)}+\tau_i}}\delta_{nm} \qquad \textbf{[S13]}$$

Combining Eqs. **S9**, [**S10**], and [**S13**], we finally obtain:

$$\tau_{DA} = \frac{\sum_n\left(\frac{\tilde{u}_A^{(n)}}{\sqrt{\xi_A}} - \frac{\tilde{u}_D^{(n)}}{\sqrt{\xi_D}}\right)^2(\tau^{(n)})^2}{\sum_n\left(\frac{\tilde{u}_A^{(n)}}{\sqrt{\xi_A}} - \frac{\tilde{u}_D^{(n)}}{\sqrt{\xi_D}}\right)^2\tau^{(n)}} + \tau_i \qquad \textbf{[S14]}$$

To fit experimental data, the model requires the following parameters: k_c, k_l, ξ_A, ξ_D, and τ_i.

The friction of the dye ξ_D can be estimated considering that a Kuhn segment in 6M GdmCl corresponds to about five amino acids resulting in a molecular mass (approximately 600 Da) similar to that of dye and linker (643 Da for Alexa488 and 820 Da for Alexa 594), such that we assume $\xi_D = \xi_A \approx \xi_s$. Fits performed with $\xi_D = 2\xi_s$ yield results that are indistinguishable within experimental uncertainty, indicating that variation of the parameter within reasonable bounds does not affect the conclusions. The dye spring constant k_l was estimated by optimizing the fit of the model to the equilibrium interdye distances obtained from FRET efficiency histograms for the variants labeled at different positions in 7 M GdmCl, where no internal friction is present and the proteins are maximally expanded. The resulting value of k_l was then used for all other fits. Note that without including the dyes and linkers explicitly, the theory predicts a rollover in the reconfiguration time as a function of segment length when $|i\text{-}j|$ approaches the total number of segments (15), which is not observed experimentally. The confining spring constant k_c was adjusted such that the change in dimensions obtained from FRET efficiency histograms at different GdmCl concentrations relative to the maximally expanded state in 7 M GdmCl was reproduced. In this way the only remaining free parameter is the internal friction time τ_i, which is obtained from fitting the model to the position dependence of the reconfiguration times (Fig. 3). The τ_i extracted with this procedure is given relative to the τ_s obtained by the model at the same GdmCl concentration. In order to compare this result with values of internal friction obtained from the viscosity dependence, the ratio $\left(\frac{\tau_i}{\tau_{ij,(i=1,j=67)}}\right)_{\text{positiondependence}}$ was multiplied by the corresponding measured reconfiguration time of the end-to-end variant, τ_r, obtained at the same GdmCl concentration. Note that the uncertainty of τ_i determined in this way increases for large values of τ_i (Fig. 4) because the deviation of τ_{ij}/τ_r from a value of 1 becomes comparable to the experimental error.

Comparison of the effects of specific and nonspecific collapse on the chain dynamics. It could be argued that simple polymer models applied to unfolded proteins, especially under near-native conditions, are too unrealistic as they fail to capture the formation of partial secondary structure or specific hydrophobic clusters within the chain. Here we use simulations to argue (1) that experimental data can be used to differentiate nonspecific collapse assumed by such models from structural ordering and (2) that our experimental results, even at the lowest denaturant concentrations, where the conditions are close to native, are more consistent with the nonspecific collapse scenario. Specifically, we have simulated a variant of the generalized Rouse model (GRM) of Thirumalai and coworkers (16, 17) to mimic the formation of specific structural order within a chain by introducing an attractive interaction between an individual pair of monomers. An example of such a computation (Fig. S7) shows that the chain segment length dependence of both the intramonomer distance $r_{ij} = \langle |\mathbf{r}_j - \mathbf{r}_i|^2 \rangle^{1/2}$ and reconfiguration time τ_{ij} found for a chain with attractive interactions between an individual pair of monomers is qualitatively different from both our experimental findings and from simple polymer models that assume nonspecific collapse. This finding suggests that specific structural ordering at low denaturant concentrations cannot explain our experimental results.

1. Nettels D, Gopich IV, Hoffmann A, Schuler B (2007) Ultrafast dynamics of protein collapse from single-molecule photon statistics. *Proc Natl Acad Sci USA* 104:2655–2660.
2. Nettels D, Hoffmann A, Schuler B (2008) Unfolded protein and peptide dynamics investigated with single-molecule FRET and correlation spectroscopy from picoseconds to seconds. *J Phys Chem B* 112:6137–6146.
3. Doose S, Neuweiler H, Sauer M (2005) A close look at fluorescence quenching of organic dyes by tryptophan. *Chemphyschem* 6:2277–2285.
4. Hoffmann A, et al. (2007) Mapping protein collapse with single-molecule fluorescence and kinetic synchrotron radiation circular dichroism spectroscopy. *Proc Natl Acad Sci USA* 104:105–110.
5. Müller-Späth S, et al. (2010) Charge interactions can dominate the dimensions of intrinsically disordered proteins. *Proc Natl Acad Sci USA* 107:14609–14614.
6. Hofmann H, et al. (2010) Single-molecule spectroscopy of protein folding in a chaperonin cage. *Proc Natl Acad Sci USA* 107:11793–11798.
7. Pfeil SH, Wickersham CE, Hoffmann A, Lipman EA (2009) A microfluidic mixing system for single-molecule measurements. *Rev Sci Instrum* 80:055105.
8. Gösch M, Blom H, Holm J, Rigler R (2000) Hydrodynamic flow profiling in microchannel structures by single molecule fluorescence spectroscopy. *Anal Chem* 72:3260–3265.
9. Schuler B (2007) Application of single molecule Förster resonance energy transfer to protein folding. *Methods Mol Biol* 350:115–138.
10. Kawahara K, Tanford C (1966) Viscosity and density of aqueous solutions of urea and guanidine hydrochloride. *J Biol Chem* 241:3228–3232.
11. Schuler B, Lipman EA, Steinbach PJ, Kumke M, Eaton WA (2005) Polyproline and the “spectroscopic ruler” revisited with single molecule fluorescence. *Proc Natl Acad Sci USA* 102:2754–2759.
12. Thirumalai D, Ha BY (1988) *Theoretical and Mathematical Models in Polymer Research*, ed Grosberg A (Academia, New York), pp 1–35.
13. Doi M, Edwards SF (1988) *The Theory of Polymer Dynamics* (Oxford University Press, USA, New York).
14. Nettels D, et al. (2009) Single molecule spectroscopy of the temperature-induced collapse of unfolded proteins. *Proc Natl Acad Sci. USA* 106:20740–20745.
15. Makarov DE (2010) Spatiotemporal correlations in denatured proteins: The dependence of fluorescence resonance energy transfer (FRET)-derived protein reconfiguration times on the location of the FRET probes. *J Chem Phys* 132:035104.
16. Barsegov V, Morrison G, Thirumalai D (2008) Role of internal chain dynamics on the rupture kinetic of adhesive contacts. *Phys Rev Lett* 100:248102.
17. Hyeon C, Morrison G, Thirumalai D (2008) Force-dependent hopping rates of RNA hairpins can be estimated from accurate measurement of the folding landscapes. *Proc Natl Acad Sci USA* 105:9604–9609.

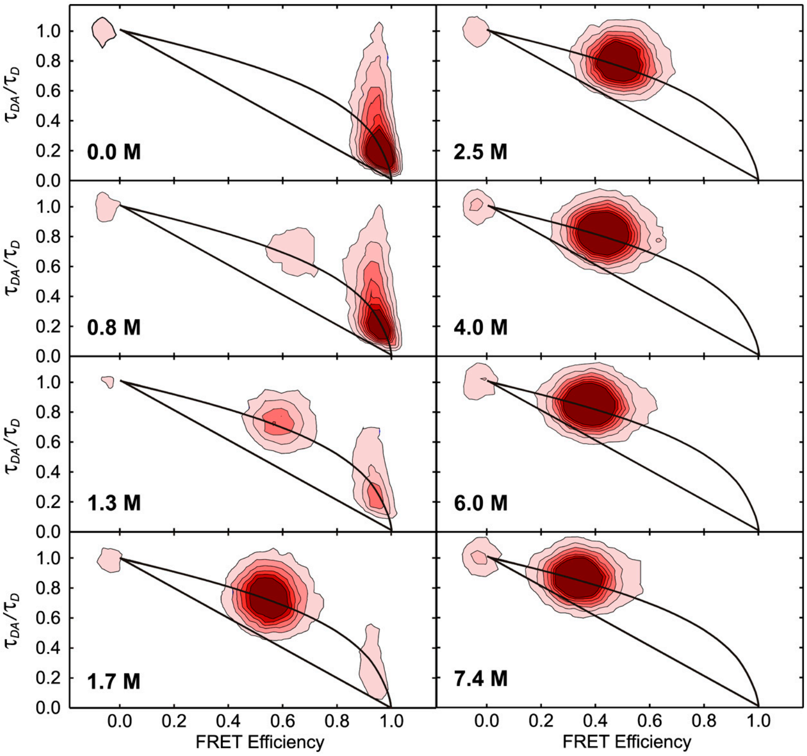

Fig. S1. Two-dimensional histograms of relative donor lifetime versus FRET efficiency measured between 0 M and 7.4 M GdmCl (cf. Fig. 1, main text). τ_{DA} and τ_D are the donor fluorescence lifetimes in presence and in absence of acceptor, respectively. For details, see *Fluorescence lifetimes and FRET efficiencies*.

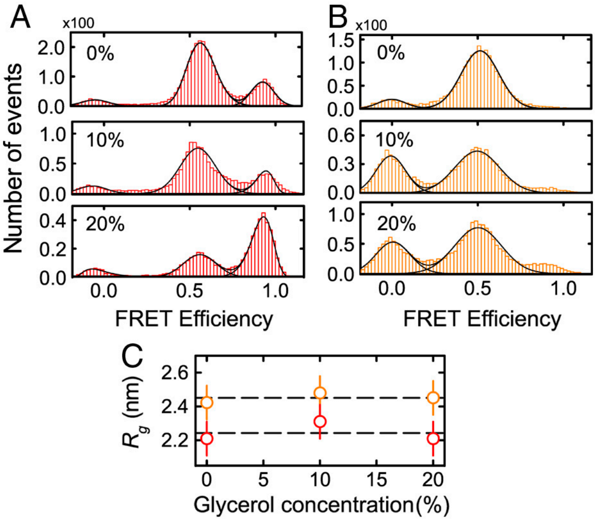

Fig. S2. FRET efficiency histograms of Csp at 1.3 M (*A*) and 2 M (*B*) GdmCl with different concentrations of glycerol (% by mass). At 1.3 M GdmCl and 20% glycerol, the denaturant concentration was adjusted slightly to 1.4 M GdmCl to counteract the effect of stabilization of the native state while maintaining the same transfer efficiency. Generally, the presence of glycerol in solution did not affect the radius of gyration of the chain significantly, as shown in (*C*) (colors as in *A*, *B*). The same behavior was observed at 4 M and 6 M GdmCl.

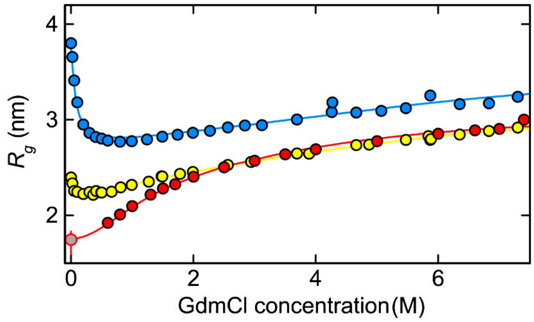

Fig. S3. Radii of gyration, R_g, for Csp (red), IN (yellow), and ProTα (blue) obtained assuming the distance distribution of a Gaussian chain. Very similar results are obtained with other distance distributions (5). The data for IN and ProTαC were fit as described previously (5). The expansion of IN and ProTα at low GdmCl concentration is due to charge repulsion at low ionic strength (5). For interpolation, the Csp data were fit with $R_g = R_{g0}(1 + \rho K_b a/(1 + K_b a))$, where R_{g0} is the dimension in the absence of denaturant, ρ is a scaling constant, K_b is an effective binding constant of denaturant to the chain, and a is the activity of the denaturant (5, 14). The residual difference in chain dimensions at high denaturant concentrations may be due to excluded volume effects from the long unlabeled polypeptide tail in ProTα or GdmCl binding to acidic side chains (5). The gray data point is from the microfluidic mixing experiment (see Fig. 4, main text).

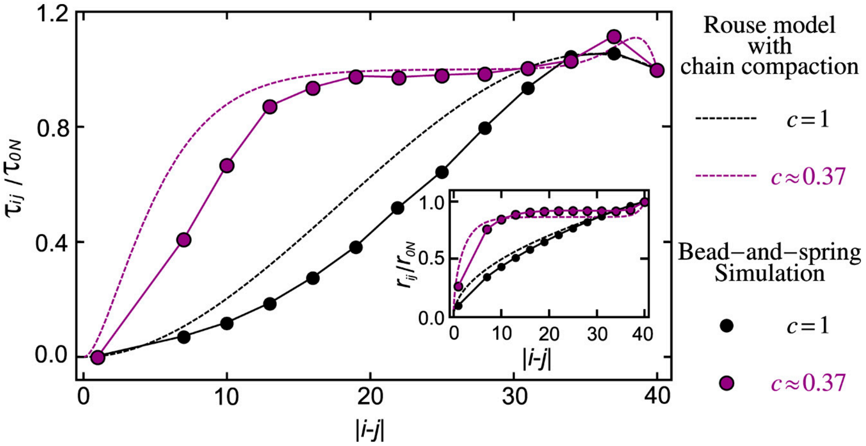

Fig. S4. Justification for using a simple harmonic potential to mimic chain collapse within the extended RIF. In the extended RIF, chain compaction is induced by applying a parabolic trapping potential to every chain monomer. Here we show that such a model realistically reproduces the properties of a chain undergoing a coil-to-globule transition. To simulate the coil-globule transition, we used a chain of $N = 41$ beads connected by harmonic springs. In addition, nonbonded beads interacted via a Lennard-Jones potential. Chain collapse was induced by lowering the temperature and quantified by the compactness parameter c equal to the ratio of the chain's root mean square distance to the root mean square distance corresponding to the high temperature limit (such that $c = 1$ at high temperature, in the absence of collapse). The reconfiguration time, τ_{ij}, and the rms distance, r_{ij}, plotted as a function of the length of the chain segment between the monomers i and j, agree well with those computed for a Rouse chain, in which collapse was introduced by applying a potential $k_c r^2/2$ to each monomer. Again, the degree of collapse for the Rouse chain was quantified by the compactness parameter c, taken, in this case, to be the ratio of the rms end-to-end distance to that for $k_c = 0$. Given the same values of the compactness parameter, the results for the Rouse model agree quite well with those for the bead-and-spring model, especially considering that the Rouse model does not take into account excluded volume effects. Here we only show the data for extreme cases of no compaction and very strong compaction (where c is smaller than the typical experimental values); similar agreement was observed for intermediate values of c (data not shown).

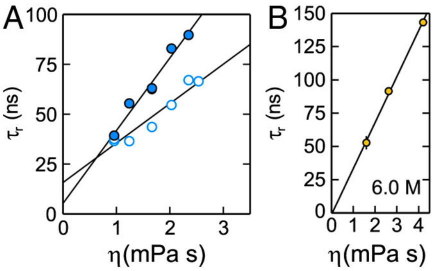

Fig. S5. (*A*) Viscosity dependence of the reconfiguration time of ProTα in native buffer (filled circles) and upon addition of 1 M KCl (empty circles). Data were fit globally as for the Csp viscosity dependence (Fig. 2), which resulted in values of the internal friction time of (6 ± 5) ns and (16 ± 3) ns without and with salt, respectively. (*B*) Viscosity dependence of the reconfiguration time of IN in 6 M GdmCl. The linear fit yields a value for the internal friction time of (-2 ± 6) ns, indicating that internal friction is negligible at high GdmCl concentrations.

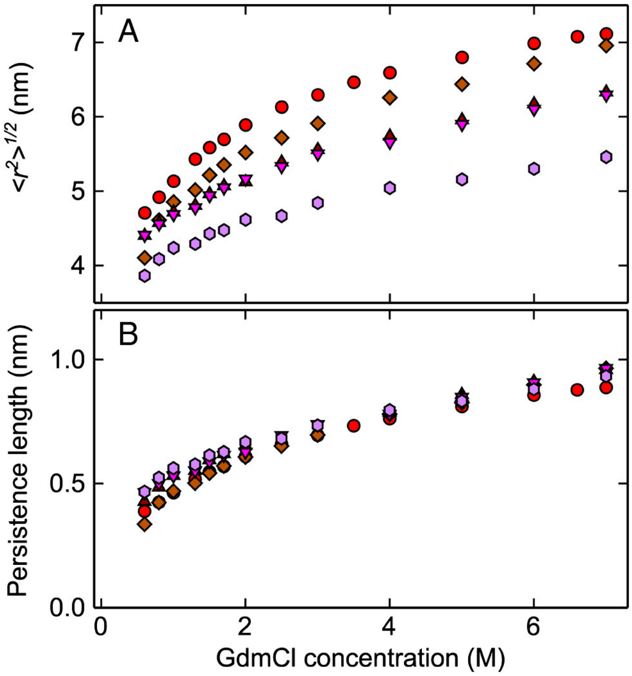

Fig. S6. Root mean squared interdye distances and persistence lengths as a function of GdmCl concentration for the different Csp variants (CspC2C68, red circles; CspC10C67 brown diamonds; CspC21C67, dark red triangles up; CspC22C67, pink triangles down; CspC36C69 violet hexagons). The good agreement of the persistence lengths indicates a uniform collapse of the chain (4) and thus the dominance of nonspecific interactions in driving collapse and causing internal friction.

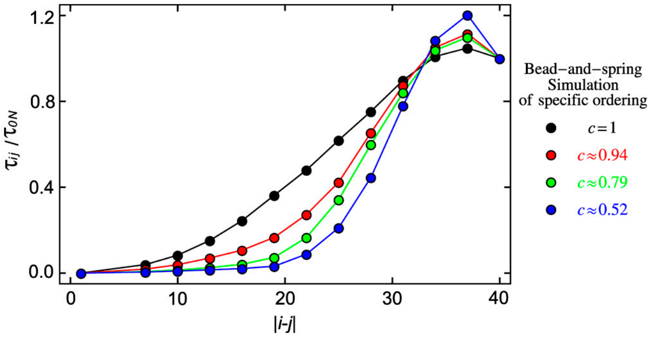

Fig. S7. Specific intrachain interactions result in spatio-temporal correlations within the polymer chain that are quite different from those observed experimentally and in simulations of nonspecific collapse. Here, we illustrate this using a generalized Rouse-type model (16, 17), in which a pair of monomers within a bead-and-spring chain model interact via an attractive potential. We use a chain with $N = 41$ beads, where the 4th and the 36th beads attract one another. We have also considered other choices of the two monomers (data not shown), leading to similar conclusions. As the strength of the attractive potential increases, more compact configurations are favored. Again, we characterize this compaction in terms of the compactness parameter c, equal to the ratio of the end-to-end distance and the end-to-end distance in the limit of no attractive interaction. The effect of chain compaction on the reconfiguration times τ_{ij} is very different from that observed in the experiments and in our simulations of chains without specific interactions (cf. Fig. S4). Specifically, more compact chains exhibit a τ_{ij} that decreases more precipitously with decreasing length of the chain segment $|i\text{-}j|$ between the monomers, in contrast to the weakening of this dependence observed experimentally at lower denaturant concentrations (Fig. 3) as well as predicted by the models that do not include monomer-specific interactions.

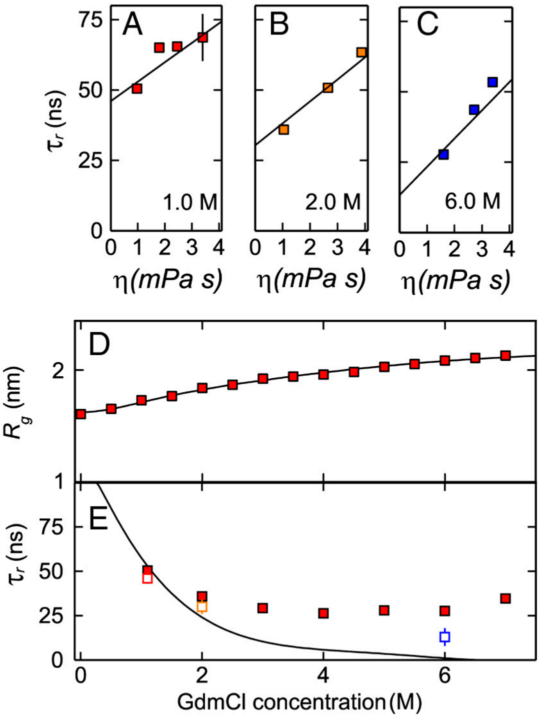

Fig. S8. Reconfiguration dynamics and internal friction of the bisected variant of CspC36C69 (see Tab. S1). Viscosity dependences of reconfiguration times, τ_r, at 1.0 M (*A*), 2.0 M (*B*), and 6.0 M GdmCl (*C*), respectively. The data were fit globally as in Fig. 2 (solid lines). (*D*) Denaturant dependence of the radius of gyration, R_g. (*E*) Reconfiguration times τ_r of the bisected variant (red filled squares) compared with the values of internal friction times obtained from the viscosity dependences (*A*–*C*) (empty squares, colors as in *A*–*C*), and with internal friction times of full length CspC2C68 (black line, from Fig. 4*A*). The good agreement of friction times in the two variants indicates the importance of local interactions for internal friction.

Table S1. Amino acid sequences of the variants of Csp from *Thermotoga maritima* used in this work (mutations relative to wt in bold, fluorophore labeling positions in bold underline)

		1 10 20 30 40 50 60
Csp(wild type)		MRGKVKWFDS KKGYGFITKD EGGDVFVHWS AIEMEGFKTL KEGQVVEFEI QEGKKGPQAA HVKVVE
CspC67	MAHHHHHHSWAALEVLFQ GPG	MRGKVK**F**FDS KKGYGFITKD EGGDVFVH**F**S AIEMEGFKTL KEGQVVEFEI QEGKKG**G**QAA HVKVVE**C**
CspC2C68	MAHHHHHHSWAALEVLFQ GPG	M**C**RGKVK**F**FD SKKGYGFITK DEGGDVFVH**F** SAIEMEGFKT LKEGQVVEFE IQEGKKG**G**QA AHVKVVE**C**
CspC10C67	MAHHHHHHSWAALEVLFQ GPG	MRGKVK**F**FD**C** KKGYGFITKD EGGDVFVH**F**S AIEMEGFKTL KEGQVVEFEI QEGKKG**G**QAA HVKVVE**C**
CspC21C67	MAHHHHHHSWAALEVLFQ GPG	MRGKVK**F**FDS KKGYGFITKD **C**GGDVFVH**F**S AIEMEGFKTL KEGQVVEFEI QEGKKG**G**QAA HVKVVE**C**
CspC22C67	MAHHHHHHSWAALEVLFQ GPG	MRGKVK**F**FDS KKGYGFITKD E**C**GDVFVH**F**S AIEMEGFKTL KEGQVVEFEI QEGKKG**G**QAA HVKVVE**C**
CspC36C69	MAHHHHHHSWAALEVLFQ GPG	MRGKVK**F**FDS KKGYGFITKD EGGDVFVH**F**S AIEGR**C**EGFK TLKEGQVVEF EIQEGKKG**G**Q AAHVKVVE**C**
CspC36C69 bisected		**C**EGFK TLKEGQVVEF EIQEGKKG**G**Q AAHVKVVE**C**

Proline was removed to eliminate a kinetic component due to cis/trans isomerization (2, 3, 16); Trp residues were replaced by Phe to eliminate static quenching of the internally labeled variants. The hexahistidine tag (blue) was removed by digest with HRV 3C protease. For CspC36C69 a Factor Xa protease site was introduced (underline) to allow preparation of a bisected variant lacking the N-terminal tail